SIGNATURE OF TROPOSPHERIC OZONE FROM FTIR OBSERVATIONS OVER TROPICAL AFRICA

A Thesis Submited in Partial Fulfillment of the
Requirments for the Degree of
Master of Science in Physics

Addis Ababa University
College of Natural and Computational Sciences
Department of Physics

MESRACH ABERA
Addis Ababa, Ethiopia
July 2016

Addis Ababa University
College of Natural and Computational Sciences
Department of Physics

The undersigned here by certify that they have read and recommend to the School of Graduate Studies for acceptance a thesis entitled "**SIGNATURE OF TROPOSPHERIC OZONE FROM FTIR OBSERVATIONS OVER TROPICAL AFRICA**" by **MESRACH ABERA** in partial fulfillment of the requirements for the degree of **Master of Science in Physics**.

Dated: July 2016

Supervisor: _____ _____

Prof. Gizaw Mengistu,
Professor, Department of Physics,
Botswana International University of Technology and Science/ AAU, AA, Ethiopia

Examiner: _____ _____

Dr. Belayneh Mesfin,
Assistant Professor, Department of Physics,
AAU, AA, Ethiopia

Examiner: _____ _____

Prof. A. V. Gholap,
Professor, Department of Physics,
AAU, AA, Ethiopia

ADDIS ABABA UNIVERSITY

Date: **July 2016**

Author: **MESRACH ABERA**

Title: **SIGNATURE OF TROPOSPHERIC OZONE FROM FTIR OBSERVATIONS OVER TROPICAL AFRICA**

Department: **Department of Physics**

Degree: **M.Sc.** Convocation: **June** Year: **2016**

Permission is herewith granted to Addis Ababa University to circulate and to have copied for non-commercial purposes, at its discretion, the above title upon the request of individuals or institutions.

Signature of Author

Dedicated with Love to:

My Mother Kokobe Negash

Wife Seble Haile

Son Fikir Mesrach

Brother Kifle Abera

Table of Contents

List of Tables

List of Figures

Abstract

The tropospheric column ozone derived from 236 measurement spectra under the condition of clear sky from May 2009 to Dec 2015 is analyzed. The main objective of this thesis is to show the high variability of tropospheric ozone over tropical Africa. For each day, ozone columns are retrieved from individual spectral measurements using PROFFIT code in the four micro windows. The tropospheric ozone obtained from the satellite is the difference between the total column of the ozone monitoring instrument/Aura with the stratospheric column obtained from microwave limb soundert/Aura. The minimum and maximum observations of tropospheric column ozone are in May 22, 2009 and January 17, 2011 respectively. In general, elevated ozone have been recorded during spring and during summer. A closer look at the spring and the summer seasons show variations among the years. The maximum ozone column amount and volume mixing ratio are recorded in March 2013, $\sim 8.5 \times 10^{17} molecule/cm^2$ and 60 ppbv respectively.

Acknowledgement

I give all the glory, honour and majesty to the Almighty God who made ways where there seemed to be no way.

I would like to express my sincere gratitude to my supervisor Prof. Gizaw Mengistu for his guidance and suggestions throughout the research period. His vast knowledge and experience shared will remain as base for my future research career

I should also praise Dilla University for covering educational fees and paying salary for the entire time of my graduate study.

I would like to thank Ato Gezahegn Sufa for his support on computational programs which have indispensable role to do my thesis. He is role model for me, specially how to manage and use time properly. I am grateful to him for investing his time to me.

I am highly indebted with all physics Departement staff and to Space and Atmospheric Physics Ph.D students in general and Ato Abera Debebe in particular in sharing their experience during the research study.

Special thanks to my brother, Kifle Abera and my wife Seble Haile, for the love, care, financial support and for being with my side throughout my study time.

May the almighty God bless you all!!!

Acronyms

FTIR	Fourier Transform Infrared Spectroscopy
OPD	Optical Path Difference
OPUS	Optical User Software
TP	Tikhonov Philips
OE	Optimal Estimation
IPCC	Intergovernmental Panel on Climate Change (WMO)
WMO	World Meteorological Organization
ZPD	Zero Path Difference
UV	Ultraviolet
CRT	Cathode Ray Tube
TCO	Tropospheric Column Ozone
DU	Dobson Units
PV	Potential Vorticity
FWHM	Full Widths at Half Maximum
TCA	Total Column Amount
RF	Radiative Forcing
UT	Upper Troposphere
AURA	Association of Universities for Research in Astronomy
OMI	Ozone Monitoring Instrument
MLS	Microwave Limb Sounder
ILS	Instrumental Line Shape
LRT	Lapse-Rate Tropopause
CPT	Cold Point Tropopause
VMR	Volume Mixing Ratio
ppmv	parts per million by volume
ppbv	parts per billion by volume
DPT	Data Point Table
PROFFIT	Profile Fit
HYSPLIT	Hybrid Single Particle Lagrangian Integrated Trajectory

Introduction

The main objective of this thesis is to show the high variability of tropospheric ozone over tropical Africa using high resolution FTIR and Aura satellite. Moreover, analysis of ozone time series, chemical and dynamical sources and sinks are investigated.

Remote sensing techniques are an indirect methods which are currently widely used for deriving atmospheric parameters such as temperature, pressure, and concentration of trace gases based on direct measurement of radiation emitted, absorbed and scattered by the atmosphere. In order to retrieve such atmospheric states inversion code based on algorithms such as SFIT2 software is employed. Retrieval algorithms requires the radiative transfer equation for modelling the observed radiance in addition to measured radiance to derive atmospheric state parameters. Radiative transfer theory (RT) employed in remote sensing application needs to describe the interaction between matter and electromagnetic radiation. There are two types of remote sensing techniques, these are passive remote sensing and active remote sensing. Passive remote sensing techniques make use of the interaction of natural radiation with the medium of interest, while active method employs artificial source of radiation such as laser source [1].

Ground-based Fourier Transform Infrared Spectroscopy is one of several instruments that provide accurate measurements of total column of many atmospheric species. In addition it has been demonstrated by several research groups that high resolution infrared spectrometers with the ability to determine the concentration of many species simultaneously

have important advantages compared to other techniques. Thus, high resolution FTIR spectroscopy has developed to an extremely valuable tool for the study of atmospheric chemistry [2].

In addition to its main components, the earth atmosphere contains atmospheric trace gases at extremely low abundance. The volume mixing ratio of these gases are also extremely low but the gases play key roles in various phenomena such as ozone depletion and global warming. Nitrogen oxides ($NO_x = NO + NO_2$) are main important atmospheric trace gases and have central importance for atmospheric chemistry. They are precursors in determining tropospheric ozone, aerosol nitrate, and the hydroxyl radical (OH) which is the main atmospheric oxidant. About two-third of the global source of NO_x is from fossil fuel combustion (IPCC, 2007) and is concentrated in urban areas. The next important source is the biomass burning in tropical areas [3].

Ozone(O_3) is considered as a pollutant at ground level and the overall effect of its exposure leads to decrease of lung capability to perform normal function. The reduction of surface ozone which is harmful to human health, animals and plants is an important objective of air quality policy for many governments. Ground level ozone is a major component of smog, produced in the troposphere by the catalytic reactions of nitrogen oxides ($NO_x = NO + NO_2$) with carbon monoxide (CO), methane (CH_4) and nonmethane volatile organic compounds (NMVOCs) in the presence of sunlight.

Exposure to elevated concentrations of surface ozone causes substantial reductions in the agricultural yields of many crops. As emissions of O_3 precursors rise in many parts of the world over the next few decades yield reductions from O_3 exposure appear likely to increase the challenges of feeding a global population projected to grow from 6 to 9 billion between 2000 and 2050. Through the absorption of infrared radiation at 9.6 nm ozone

also acts as a greenhouse gas which has implications for the global climate. Even though the warming effect of ozone is small compared to gases such as CO_2, methane, and water vapor, at $\sim$0.35 Wm^{-2} it is still significant [4].

Chapter 1

The Earth‘s Atmosphere, Structure and Chemistry

The earth's atmosphere consists of a mixture of gases, mostly molecular nitrogen (78% by volume) and molecular oxygen (21% by volume) (see Table 1.1). Argon water vapor, carbon dioxide and ozone along with other minor constituents, comprise the remaining 1% of the atmosphere. Although they appear in very small abundances, trace species like water vapor and ozone play a key role in the energy balance of the earth through involvement in radiative processes. Because they are created and destroyed in particular regions and are linked closely to the circulation through transport, these and other minor species are highly variable. For this reason, such species are treated separately from the primary atmospheric constituents, which are referred to simply as "dry air" [5].

1.1 Chemical Composition of the Atmosphere

The objective of atmospheric chemistry is to understand the factors that control the concentrations of chemical species in the atmosphere. The atmosphere is a relatively stable mixture of gases, during the day, the proportion of which, excluding water vapor are uniform up to approximately 80 km above the Earth's surface [7].

The major components of the atmosphere by volume are oxygen, nitrogen and argon, which have not varied significantly in abundance over the last several millenia at least and are not expected to vary much in the foreseeable future. Further- more, these three gases each contain atoms of a single element and so possess molecular symmetries that prevent them from absorbing or emitting infrared radiation under most conditions of temperature and pressure found in the Earth's atmosphere. These gases do affect the propagation of solar radiation through the process of Rayleigh scattering and hence contribute to global cooling of the planet despite the fact that they do not contribute directly to the greenhouse effect. They do moderate the greenhouse effect indirectly, as the atmospheric pressure they produce affects the efficiency by which the infrared active molecules absorb the Earth's thermal radiation emitted to space.

The atmosphere is thought of as a dynamic system, with its gaseous constituents continuously being exchanged with vegetation, oceans and biological organisms. The cycle of atmospheric gases involve a number of physical and chemical processes. Gases are produced chemically by biological activity, volcanic eruption, radioactive decay and human activity, while, removal is through chemical reactions, physical processes and deposition. Also present are a number of trace gases that occur relatively in small amount and sometimes highly variable amounts. Even with this remarkably small composition, temperature and atmospheric chemistry are believed to be controlled by the trace gases. There is evidence that environmentally significant trace gases are changing because of both natural and human factors. Carbon dioxide (CO_2), nitrous oxide (N_2O) and methane (CH_4) are changing in concentration through actions like the burning of fossil fuels, biomass burning, release from metabolic processes of micro-organisms in the soil, industries, traffic and oceans of the planet. In the present terrestrial atmosphere, the trace gases, water vapor (H_2O), carbon dioxide (CO_2), methane (CH_4), nitrous oxide (N_2O) and ozone (O_3), are the main greenhouse gases [7].

The man made chlorofluorocarbons (CFCs), associated with cosmic sprays and refrigeration also contribute to the present greenhouse effect. These are minor constituents of the atmosphere in terms of abundance, and, unlike the major constituents, these abundances are prone to change. CO_2, CH_4, N_2O and CFCs have increased systematically within the past century[5]. Water vapor abundance is largely controlled by the ocean surface, temperature and transport processes, and the global distribution of its atmospheric concentration is highly variable. There is increasing evidence that the percentages of trace gases are changing because of both natural and human factors. Some of the gases do not have uniform mixing ratios (e.g. ozone, water vapor, etc.) in the lowest 100 km. They can have a source at the surface or in the atmosphere or, a sink at the surface or in the atmosphere. If the lifetime of gas is shorter than the time it takes to get transported from one place to another, then the gas may not be uniformly distributed throughout the atmosphere. Table 1.1 lists the mixing ratios of some major atmospheric gases. As shown in the Table, minor constituents at low levels of the atmosphere may include variable quantities of dust, smoke and toxic gases and vapors such as sulfur dioxide, methane, oxides of nitrogen etc, some of which pollute the atmosphere and are highly toxic.

Table 1.1: Atmospheric Composition [6].

Constituent	Tropospheric mixing ratio	Vertical distribution (mixing ratio)	Controlling processes
N_2	0.7808	Homogeneous	Vertical mixing
O_2	0.2095	Homogeneous	Vertical mixing
H_2O^b	≤ 0.030	Decreases sharply in troposphere; increases in stratosphere; highly variable	Evaporation, condensation, transport; production by CH_4 oxidation
Ar	0.009	Homogeneous	Vertical mixing
CO_2^b	345 ppmv	Homogeneous	Vertical mixing;production by surface and anthropogenic processes
O_3^b	10 ppmv	Increases sharply in stratosphere; highly variable	Photochemical production in stratosphere; destruction at surface transport
CH_4^b	1.6 ppmv	Homogeneous in troposphere; decreases in middle atmosphere	Production by surface processes; oxidation produces H_2O
N_2O^b	350 ppbv	Homogeneous in troposphere decreases in middle atmosphere	Production by surface and anthropogenic processes; dissociation in middle atmosphere; produces NO transport
CO^b	70 ppbv	Decreases in troposphere; increases in stratosphere	Production anthropogenically and by oxidation of CH_4 transport
NO	0.1 ppbv	Increases vertically	Production by dissociation of N_2O catalytic destruction of O_3
$CFC-11^b$	0.2 ppbv	Homogeneous in troposphere;	Industrial production; mixing in troposphere;
$CFC-12^b$	0.3 ppbv	decreases in stratosphere;	photodissociation in stratosphere

[b]Radiatively active

1.2 Regions and Characteristics of the Atmosphere

In the most general terms, the atmosphere is divided into lower and upper regions. The lower atmosphere is generally considered to extend to the top of the stratosphere, an altitude of about 50 kilometers (km).

The earth's atmosphere is characterized by variations of temperature and pressure with height. In fact, the variation of the average temperature profile with altitude is the basis for distinguishing the layers of the atmosphere. The regions of the atmosphere are shown in Fig.1.1. Almost all weather phenomena occurs in the troposphere, the lowest layer of the atmosphere, which extends from the surface up to 8 to 16 kilometers above Earth's surface (lowest toward the poles, highest in the tropics) [8].

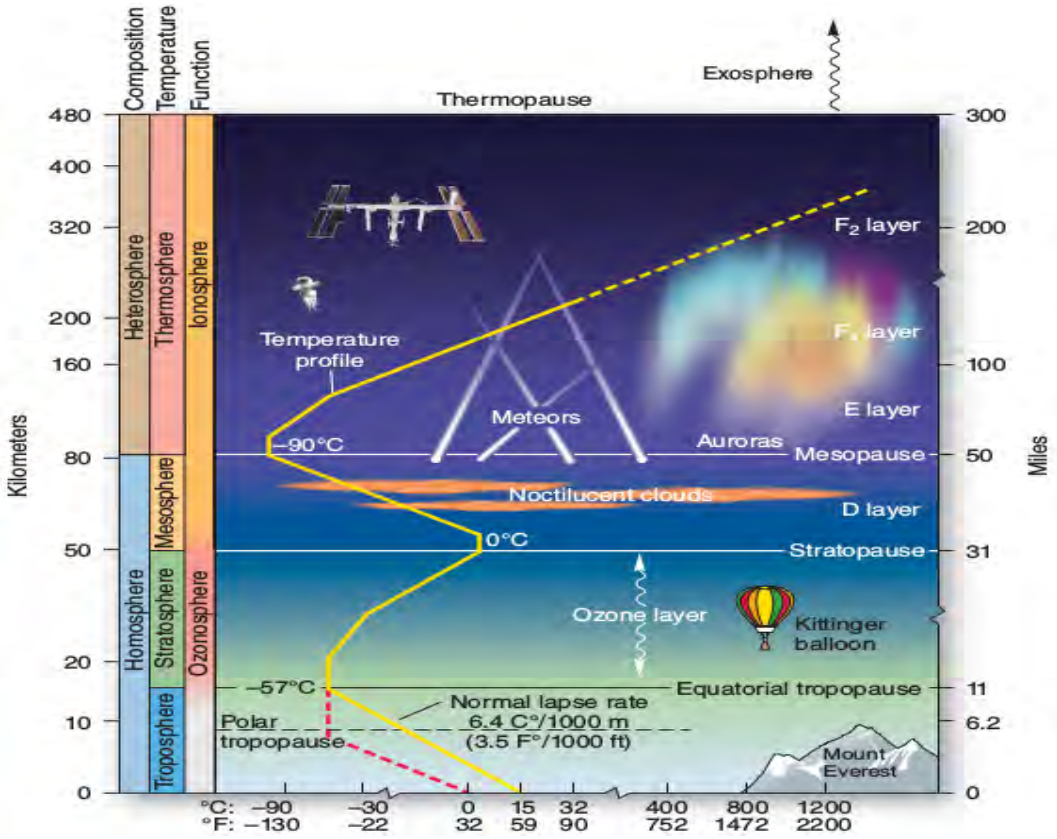

Figure 1.1: The layers of the atmosphere. The columns along the left side show the division of the atmosphere by composition, temperature and function. The plot of temperature by altitude refers to the scale along the bottom axis [9].

The atmosphere is categorized according to its thermal structure, which determines the dynamical properties of individual regions. The simplest picture of the atmosphere's thermal structure is provided by the vertical profile of global mean temperature in Fig.1.1. From the surface up to about 10 km, temperature decreases with altitude at a nearly constant lapse rate, which is defined as the rate of "decrease" of temperature with altitude. This layer immediately above the earth's surface is known as the *troposphere*, which means "turning sphere" and symbolizes the convective overturning that characterizes this region. Having a global mean lapse rate of about 6.5 K km^{-1}, the troposphere contains most of what is known as weather and is driven ultimately by surface heating[6].

The upper boundary of the troposphere or "tropopause" lies at an altitude of about 10 km (100 mb) and is marked by a sharp change of lapse rate. The region from the tropopause to an altitude of about 85km is known as the *middle atmosphere*. Above the tropopause, temperature first remains nearly constant and then increases in the stratosphere, which means "layered sphere"and is symbolic of properties at these altitudes[6].

Increasing temperature with altitude (negative lapse rate) in the stratosphere reflects ozone heating, which results from the absorption of solar UV. Contrary to the troposphere, the stratosphere involves only weak vertical motions and is dominated by radiative processes. The upper boundary of the stratosphere or "stratopause" lies at an altitude of about 50 km (1 mb), where temperature reaches a maximum. Above the stratopause, temperature again decreases with altitude in the mesosphere, where ozone heating diminishes. Convective motions and radiative processes are both important in the mesosphere. Meteor trails form in this region of the atmosphere, as do lower layers of the ionosphere during daylight hours. The "mesopause" lies at an altitude of about 85 km (0.01 mb), where a second minimum of temperature is reached. Above the mesopause, temperature increases steadily in the thermosphere (compare Fig.1.1). Unlike lower regions, the thermosphere cannot

be treated as an electrically neutral continuum. Ionization of molecules by energetic solar radiation produces a plasma of free electrons and ions, each of which interacts differently with the earth's electric and magnetic fields. As is apparent in Fig.1.1, this region of the atmosphere is influenced strongly by variations of solar activity. However, its influence on processes below the mesopause is very limited [6].

1.3 Radiative Transfer in the Atmosphere

1.3.1 Extinction and Emission

Matter and radiation have only two forms of interactions: extinction and emission. Lambert first proposed that the extinction (i.e, reduction) of radiation traversing an infinitesimal path ds is linearly proportional to the incident radiation and the amount of interacting matter along the path:

$$\frac{dI_v}{ds} = -k(v)I_v \tag{1.3.1}$$

where k(v) is the extinction coefficient, a measurable property of the medium, and ds is the absorber path length. k(v) is proportional to the local density of the medium and is positive definite. Extinction includes all processes which reduce the radiant intensity.

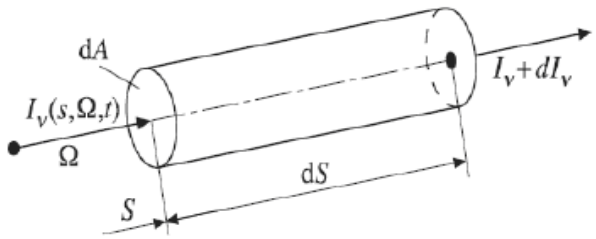

Figure 1.2: Schematic presentation of the total energy transformation by a volume element.

These processes include absorption and scattering, both of which remove photons from the incident beam. Similarly the radiative emission is also proportional to the amount of

matter along the path:

$$\frac{dI_v}{ds} = k(v)S_v \tag{1.3.2}$$

where S is known as the source function. The source function plays an important role in radiative transfer theory. Emission includes all processes which increase the radiant intensity. These processes include thermal emission and scattering which adds photons to the beam.

Extinction and emission are linear processes, and thus additive. Since they are the only two processes which alter the intensity of radiation, they can be combined as:

$$\frac{dI_v}{ds} = -kI_v + kS_v \tag{1.3.3}$$

$$\frac{1}{k}\frac{dI_v}{ds} = -I_v + S_v \tag{1.3.4}$$

Eq.(1.3.4) is the differential equation of radiative transfer in its simplest form

1.3.2 Optical Depth

Optical depth is a dimensionless parameter which quantifies the attenuation of the suns direct beam. It is a measure of how much light do air born particles prevent from passing through a column of atmosphere. Aerosols tend to absorb or reflect the incoming sunlight, thus reduce visibility and increase optical depth. Optical depth of less than 0.1 indicates a crystal clear sky with maximum visibility whereas the value 4 indicates the presence of aerosol so dense which is difficult to see the sun at mid-day. Mathematically, we define optical depth τ between points P_1 and P_2 as:

$$\tau(z_1, z_2) = \int_{z_1}^{z_2} k dz \tag{1.3.5}$$

or, in differential form:

$$d\tau = -kdz \tag{1.3.6}$$

1.3.3 Radiative Transfer Equation in Stratified Atmosphere

A stratified atmosphere is one in which all atmospheric properties such as temperature, density, etc vary only vertically. We obtain the radiative transfer equation in terms of optical depth as, [12]

$$U\frac{dI_v}{d\tau} = -I_v + S_v \tag{1.3.7}$$

where the photon path increment ds at polar angle in a stratified atmosphere is related to the vertical path increment dz by dz = cosds or ds = $U^{-1}dz$ is used in Eq. (1.3.3). Eq. (1.3.7) is the differential form of the radiative transfer equation in a plane parallel atmosphere for all angles.

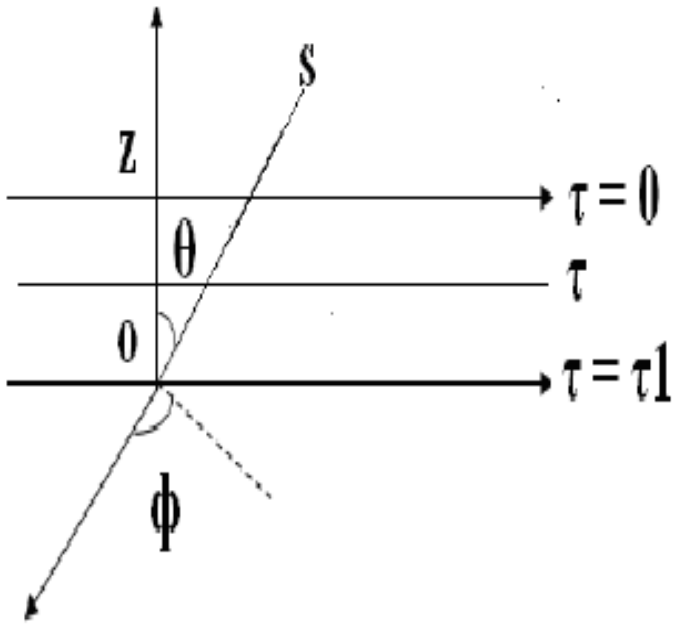

Figure 1.3: Geometry for plane parallel atmosphere.

We know that at the top of the atmosphere, sunlight is the only incident intensity from the hemisphere containing the sun; and at the surface, we have constraints on the upwelling intensity due to thermal emission or the surface reflectivity. When combined, these two hemispheric boundary conditions span a complete range of polar angle.

Thus we need to decouple Eq. (1.3.7) into its constituent upwelling and down welling

radiation components [12].

$$-\mu\frac{dI_v^-}{d\tau} = I_v^- - S_v^- \tag{1.3.8}$$

$$-\mu\frac{dI_v^+}{d\tau} = I_v^+ - S_v^+ \tag{1.3.9}$$

Eq. (1.3.8) is defined over $0 < \theta < \frac{\pi}{2}$ and Eq. (1.3.9) is defined over $\frac{\pi}{2} < \theta < \pi$ where I_v^- and I_v^+ are down welling and upwelling radiance, similarly for source functions S_v^- and S_v^+, and $\mu = \parallel U \parallel = \parallel cos \parallel$ which is a positive definite. These are the equations of radiative transfer in slab geometry for down welling ($0 < \theta < \frac{\pi}{2}$) and upwelling ($\frac{\pi}{2} < \theta < \pi$) intensities, respectively. The solution for down welling radiance is given by

$$I_v(\tau, -\mu) = \exp\frac{-\tau}{\mu} I_v(0, -\mu) + \mu^{-1}\int_0^\tau \exp\frac{-(\tau - \tau')}{\mu} S_v(\tau', -\mu)d\tau' \tag{1.3.10}$$

The solutions for radiative transfer equation are important for applications in remote sensing of the atmosphere, and calculation of radiative forcing [12].

Chapter 2

Atmospheric Ozone (O_3)

Ozone is critical to life on earth because it blocks harmful UV radiation from the Sun reaching the surface. Ozone absorbs harmful UV radiation from the Sun in the 200-300 nanometer (i.e. 2-3 x 10^{-7} meter) wavelength region. In so doing, ozone is responsible for life as we know it. Ozone is formed 10 to 40 kilometers above the ground in a region where intense UV radiation from the Sun breaks apart (photodissociates) the diatomic oxygen molecule O_2. Absorption of solar radiation occurs in the stratosphere, causing it to be warmer than it would otherwise be. Indeed, it is because of this ozone layer that the temperatures rise with height, giving rise to the structure of the stratosphere. It is contrasted with the troposphere ozone is also produced at the surface in two ways [13], both of which are related to human activities. One way is in the form of photochemical smog that arises from industrial pollution reacting with sunlight. Another is in so-called "biomass burning". This refers to burning of jungle, savannah, and existing farm land. It is primarily due to human agricultural needs, though lightening can also trigger wildfires that result in biomass burning-related ozone creation. These forms of ozone are unhealthy, while stratospheric ozone, by blocking dangerous UV light, is essential for life on Earth's surface. Our focus here is on this beneficial ozone created by energetic UV light, principally in the stratosphere [13]. About 90% of the ozone in our atmosphere is contained in the stratosphere, the region from about 10 to 50-km above Earth's surface.Ten percent(10%) of the ozone is contained in the troposphere.

Measurements taken from instruments on the ground, flown on balloons, and operating in space show that ozone concentrations are greatest between about 15 and 30 km. The yellow curve in Fig.2.1 shows how ozone amount varies with altitude. This sort of plot is called a vertical profile [13]. In contrast to beneficial stratospheric ozone, tropospheric

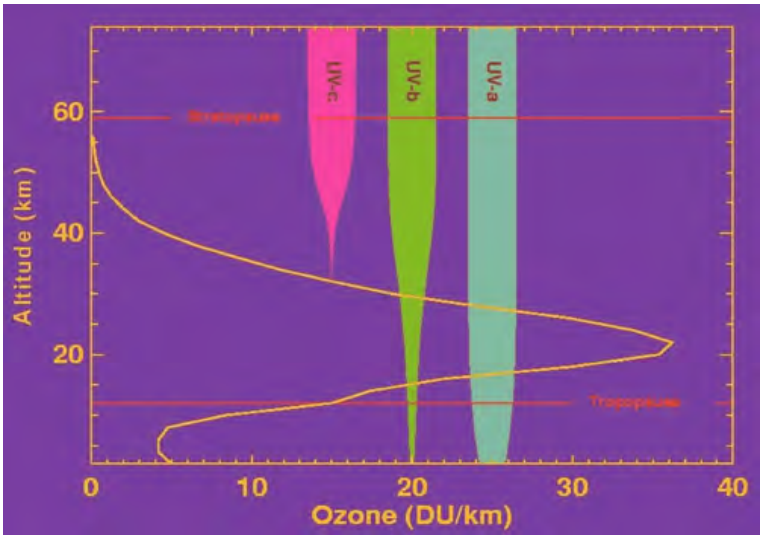

Figure 2.1: Vertical Profile of Ozone [13].

ozone is a pollutant found in high concentrations in smog. Though it too absorbs UV radiation, breathing it in high levels is unhealthy, even toxic. The high reactivity of ozone results in damage to the living tissue of plants and animals. This damage by heavy tropospheric ozone pollution is often manifested as eye and lung irritation. Tropospheric ozone is mainly produced during the day time in polluted regions such as urban areas. Significant government efforts are underway to regulate the gases and emissions that lead to this harmful pollution, and smog alerts are regular occurrences in polluted urban areas [13].

2.1 Tropospheric Ozone O_3 (TCO)

TCO is defined as the integrated amount of ozone in a vertical column of air between Earth's surface and the tropopause. It is measured in Dobson Units, where 1 DU is 2.687×10^{16} molecules per square centimetre of the column cross section [14].

Tropospheric ozone is a trace gas with a large natural variability in space and time and a mixing ratio in the range of about 10 - 100 ppbv [15]. A measure of TCO was obtained by integrating the averaged ozone profiles between the surface (sfu) and a predetermined height of 12 km (above sea level). The method used to compute integrated TCO is based on ozone readings in ppbv at available levels [20]. The conversion to DU at each level was estimated as follows:

$$O_{DU} = \frac{(O_{ppbv}/10^{-9}) \times P \times \Delta H \times 273.15 \times 1000}{1013.25 \times T_k} \tag{2.1.1}$$

where O_{ppbv} = ozone concentration (ppbv), O_{DU} = ozone in Dobson units, T_K = temperature (K) ΔH = [Difference in height between 2 successive layers (geopotential metres)]/2, and p = pressure (hPa) [20].

TCO was subsequently subdivided into four layers within the troposphere, namely, sfc-3 km, 3-5, 5-7 and 7-12 km, in order to investigate the factors responsible for TCO variations. The layers were selected on the basis of the work of Cosijn and Tyson [16] on absolutely stable layers over southern Africa, which occur preferentially at approximately 700 hPa (3 km), 500 hPa (5 km) and 300 hPa (7 km). Various methods exist for determining the upper level below which ozone may be integrated. Ideally, this height should represent the tropopause, which is known to vary on a seasonal and a daily basis. Some studies define a dynamic tropopause that is based on a change in PV. Others define a thermal tropopause based on the vertical temperature gradient. Yet others define a chemical tropopause that is based on the height at which ozone shows a sudden increase. Related to this last approach is one in which an ozone threshold of 100 ppbv was used to distinguish stratospheric air from tropospheric air. Integrated tropospheric ozone in each of four layers reveals the same spring maximum in each layer. Below 5 km, the TCO minimum occurs in February and March, whereas above 5 km, the minimum is evident in April and May. These results suggest a decoupling of the atmosphere and emphasize the important role of the 5 km absolutely stable layer in the accumulation and dispersal

of atmospheric pollutants [20]. Full troposphere and UT O_3 burdens are distinguished because O_3 in the UT has a higher RF efficiency on a per molecule basis [20]. The UT is defined from 500 hPa to the tropopause, where the tropopause is identified at the 150 ppbv O_3 level [20].

2.1.1 Ozone Precursors

The spatial and temporal distribution of ozone and its precursors are in large part driven by the distribution of their emissions. An accurate knowledge of the surface emissions and of their evolution with time is therefore essential to support the analysis and modelling of air quality and climate change interactions. Up-to-date and consistent emissions are moreover required for the forecasting of the atmospheric composition [20]. Gridded global, regional and national emission estimates exist for many of the pollutants that are important for understanding and analysing the distribution of ozone and its precursors, i.e.NO_x, CO, CH_4 and volatile organic compounds (VOC_s). Some of these inventories are publicly available,whereas others are developed by individual research groups or government agencies to study specific aspects of emissions or atmospheric processes and are not always easy to access [20]. Photochemical smog arises when sunlight acts on a mixture of nitrogen oxides and (VOC_s) producing ozone, other oxidants and aerosol. The key chemical pathway in this is the oxidation of nitric oxide (NO) by alkyl peroxy radicals (RO_2) to form nitrogen dioxide (NO_2) which then leads to ozone (O_3) production [21].

$$RO_2 + NO \rightarrow RO + NO_2 \qquad R2.1$$

$$NO_2 + h\nu + O_2 \rightarrow NO + O_3 \qquad R2.2$$

The chemical factors that control the ozone production in photochemical smog are the availability of RO_2 and NO. The availability of RO_2 is dependent on the concentration of primary (VOC_s) in the air, and the concentration of secondary oxidation products formed from these primary (VOC_s). In many cases, the secondary oxidation products are more photochemically active than the primary VOC emissions [22].

2.1.2 Ozone Production in the Troposphere

Ozone can form by the recombination of an oxygen molecule and an oxygen atom, similarly as in the stratosphere.Nevertheless,O atom cannot form in the troposphere by the photodissociation of molecular oxygen,because this reaction requires short wavelength ($\lambda < 242nm$) which is not available in the troposphere (due to the absorption by stratospheric ozone).In the troposphere, nitrogen dioxide is the only known compound that can produce O atom during its photodissociation at available radiation [23]:

$$NO_2 + h\nu(\lambda < 420) \rightarrow O + NO \qquad R2.3$$

$$O + O_2 + M \rightarrow O_3 + M \qquad R2.4$$

In the presence of NO, O_3 reacts with it, which reaction destroys the ozone and reproduces the NO_2:

$$O_3 + NO \rightarrow O_2 + NO_2 \qquad R2.5$$

This means that reaction (R2.3)(R2.5) themselves do not result net ozone production, because these reactions only recycle O_3 and NO_x. Net ozone production occurs, when other precursors, such as carbon monoxide (CO), methane (CH_4), non-methane hydrocarbons (NMHC) or certain other organic compounds (volatile organic compounds VOC) are present in the atmosphere. Ozone production can be simulated by a simple reaction scheme, through the oxidation of carbon monoxide, when nitric oxide is available. In this reaction chain OH, HO2, NO and NO2 participate as catalysts [23]:

$$CO + OH \rightarrow H + CO_2 \qquad R2.6$$

$$H + O_2 + M \rightarrow HO_2 + M \qquad R2.7$$

$$HO_2 + NO \rightarrow OH + NO_2 \qquad R2.8$$

$$NO_2 + h\nu(\lambda < 420) \rightarrow O + NO \qquad R2.3$$

$$O + O_2 + M \rightarrow O_3 + M \qquad R2.4$$

net:

$$CO + 2O_2 \rightarrow CO_2 + O_3 \qquad R2.9$$

Similar reactions chain occurs with the oxidation of methane in NO rich environment, when ozone

and formaldehyde (CH_2O) are formed rapidly [23]:

net:

$$CH_4 + 4O_2 + 2h\nu \rightarrow CH_2O + H_2O + 2O_3 \qquad R2.10$$

Formaldehyde fotodissociates to generate other radicals, which can participate further ozone productions [23].

Instead of methane, other organic compounds (NMHC,VOC) can also be participated in this reaction chain, where carbonyl species or a ketone formed next to the ozone. A schematic pattern of tropospheric ozone production can be seen in Fig.2.2 [23].

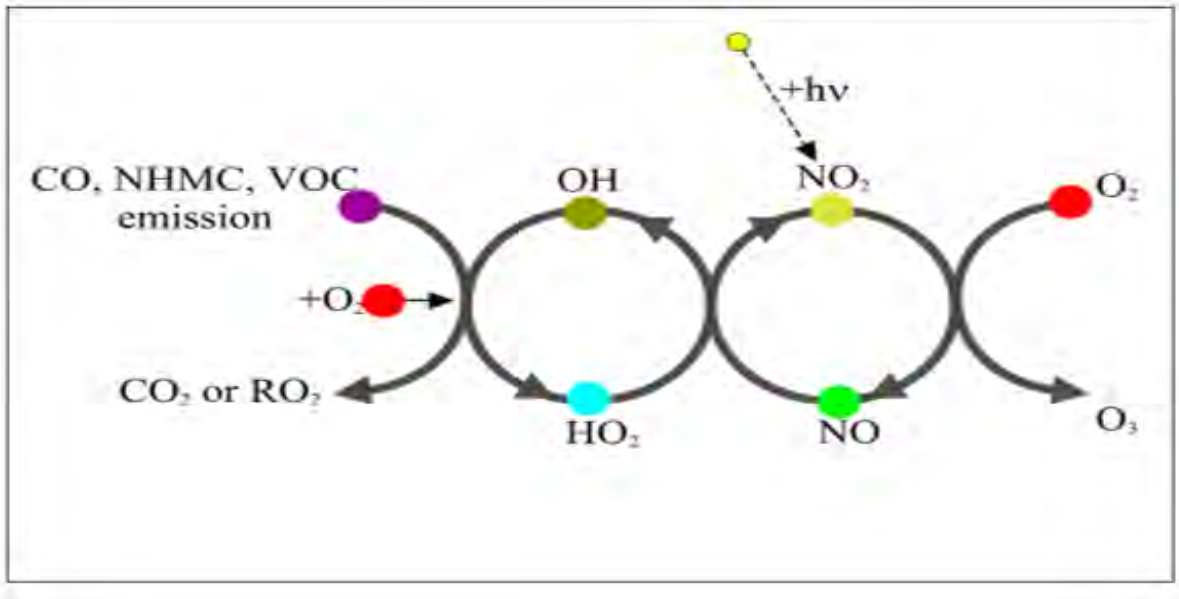

Figure 2.2: Schematic picture of photochemical ozone formation in the troposphere [23].

2.1.3 Sinks of the Tropospheric Ozone

Primary loss processes of tropospheric ozone are the photochemical reaction $O_3 + h\nu(\lambda < 320) \rightarrow O_2 + O$,when O_3 molecules dissociate by solar radiation. In NO rich environment, the reaction (R2.5) governs the ozone destruction. On the other hand, in NO-poor environment, the oxidation of carbon dioxide can lead to ozone loss. In that case, after the reactions (R2.6) and (R2.7) the generated HO_2 can react with ozone (instead of

reaction R2.8) [23]:

$$HO_2 + O_3 \rightarrow OH + 2O_2 \qquad R2.11$$

Further ozone can be destroyed by the direct reaction with OH radical:

$$OH + O_3 \rightarrow HO_2 + 2O_2 \qquad R2.12 \text{ [23]}$$

2.1.4 Transport and Mixing Processes

Research over the past two decades has clearly shown that ozone and ozone precursors are regularly exported from their emission source, or point of production, to receptor regions far downwind on the regional, intercontinental and even hemispheric scale. These transport pathways are predominantly from west to east at mid-latitudes, with in situ and satellite-based observations showing that pollution plumes (anthropogenic and biomass burning) not only travel from North America to Europe, or from East Asia to North America, but can also circle the globe [21].

Chapter 3

TCO Climatology and Sources over Africa

TCO concentration increases towards higher latitude from the equator. At the northern tip of Africa, ozone concentration peaks in April,and shifts from April to September near the equator. Ozone concentration peaks during the period from June to October, and decreases afterwards over Southern Africa [15].

The tropospheric ozone burden varies seasonally as measured by the remotely sensed AURA OMI/MLS tropospheric column product [16]. The region of the Earth with the strongest seasonal ozone variation is the northern mid-latitudes where the ozone burden is at a minimum in October and November and then increases by 30 % through winter and spring until it reaches a maximum in June [17]. Much of this seasonal variability can be explained by the flux of ozone from the stratosphere to the troposphere with a Northern Hemisphere peak flux in May and a minimum flux in November occurring predominantly in mid-latitudes [18]. Until recently ozone transport from the stratosphere to the troposphere was believed to be dominated by processes such as tropopause folds and gravity wave breaking, with little attribution given to deep convection [19]. However, a new model-based estimate that accounts for deep convection penetrating the lowermost stratosphere increases the Northern Hemisphere peak stratosphere-to-troposphere ozone flux by 19 % and shifts the peak month from May to June. Sudden STE events are well

known to influence ground-based ozone measurements over a short period [21].

Africa is an important source region for O_3 precursors [25]. It emits a large amount of biomass burning (BB) emissions (CO, NO_x, VOC_s) associated with savanna and forest fires, which take place during dry (December to February, DJF) and monsoon (June to August, JJA) periods over West and Central Africa respectively, as well as with agricultural waste and domestic biofuel combustion [26], [27], [28]. Furthermore, vegetation and soils are also considered to be important sources of O_3 precursors over Africa [29].Forests and savanna near African Equatorial regions release large amounts of VOCs [30], particularly isoprene, terpenes and methanol which are the dominant VOC emissions from vegetation. Important amounts of nitric oxide (NO) are emitted by soils after rainfall events over the Sahel region during the summer monsoon [31]. Analysis of satellite NO_2 data by [32] showed enhancements in NO_2 columns over this region during the monsoon season also attributed to rain induced emissions of NO_x from soils. Using surface NO_2 data collected over Banizoumbou (Niger) between 1998 and 2004, [33], also showed increased NO_2 concentrations dur- ing the monsoon season. African cities along the southern coast and industrialized countries (e.g. Nigeria) release important amounts of anthropogenic emissions , related to oil gas exploration, which can influence regionally [31] [35].

Dynamical processes strongly influence ozone and precursor distributions in the African troposphere. During the Northern Hemisphere summer monsoon season, West Africa is marked by intense convective activity that occurs around the Inter Tropical Convergence Zone (ITCZ) around 10°N. The resulting mesoscale convective systems (MCSs) lead to vertical transport of air masses, more or less influenced by local emissions, into the upper troposphere (UT) where chemical species have longer lifetimes and can be redistributed globally by prevailing westward winds. Using aircraft measurements performed in the framework of the African Monsoon Multidisciplinary Analyses (AMMA) project, showed

clear signatures of convective uplift of CO and aerosols into the tropical tropopause layer (TTL). Results from [34] also pointed to convection as an explanation for observed enhancements of VOCs in the UT over West Africa. Moreover, [36] [37], demonstrated that convection leads to production of important amounts of NO_x from lightning in the UT which subsequently leads to O_3 production downwind [38].

During the summer monsoon, biomass burning(BB) emissions occur mostly south of the Equator over Central Africa. Nevertheless, cross-hemispheric transport of these emissions into West Africa has been shown to occur particularly during phases when the southern branch of the African Easterly Jet (AEJ) is active [39]. This allows transport of BB pollutants towards the southern coast of West Africa in the lower/mid troposphere. BB pollution can also be transported northwards into active convective regions over Chad/Sudan where they can be uplifted into the UT and transported westwards. Evidence for this pathway was found in analysis of aircraft data collected in the UT over West Africa. Recent studies have suggested an important role for import of Asian emissions on the chemical composition of the African UT during boreal summer [40]. As shown for example by Park et al. (2009), convection associated with the Indian monsoon leads to injection of Asian trace gases into the UT. The Tropical Easterly Jet (TEJ) at 200 hPa that extends into the Atlantic Ocean [41] allows rapid westward transport of Asian pollution to West Africa [40]. Analyzed transport of tagged Asian O_3 tracers in their global models. Both studies showed O_3 outflow in the UT from Asia towards Africa. Analysis of pathways of intercontinental transport in summer performed within the HTAP (Hemispheric Transport of Air Pollution; see http://www.htap.org) project using passive CO tracers released over the northern hemisphere continents also confirmed that Asian pollution can reach the African UT [38].

Chapter 4

Instrumentation and Methodology

4.1 Instrumentation

4.1.1 The FTIR

Spectroscopy is the study of the wavelength distribution of radiation from a sample that can be used to identify the characteristics of atoms or molecules in the sample. Infrared spectroscopy is particularly important to organic chemists in analyzing organic molecules. Traditional spectroscopy involves the use of an optical element, such as a prism or a diffraction grating, which spreads out various wavelengths in a complex optical signal from the sample into different angles. In this way, the various wavelengths of radiation and their intensities in the signal can be determined. These types of devices are limited in their resolution and effectiveness because they must be scanned through the various angular deviations of the radiation.

The technique of Fourier Transform Infrared Spectroscopy (FTIR) is used to create a higher-resolution spectrum in a time interval of one second that may have required 30 minutes with a standard spectrometer. In this technique, the radiation from a sample enters a Michelson interferometer. The movable mirror is swept through the zero-path-difference condition and the intensity of radiation at the viewing position is recorded. The result is a complex set of data relating light intensity as a function of mirror position,

called an interferogram. Because there is a relationship between mirror position and light intensity for a given wavelength, the interferogram contains information about all wavelengths in the signal [42].

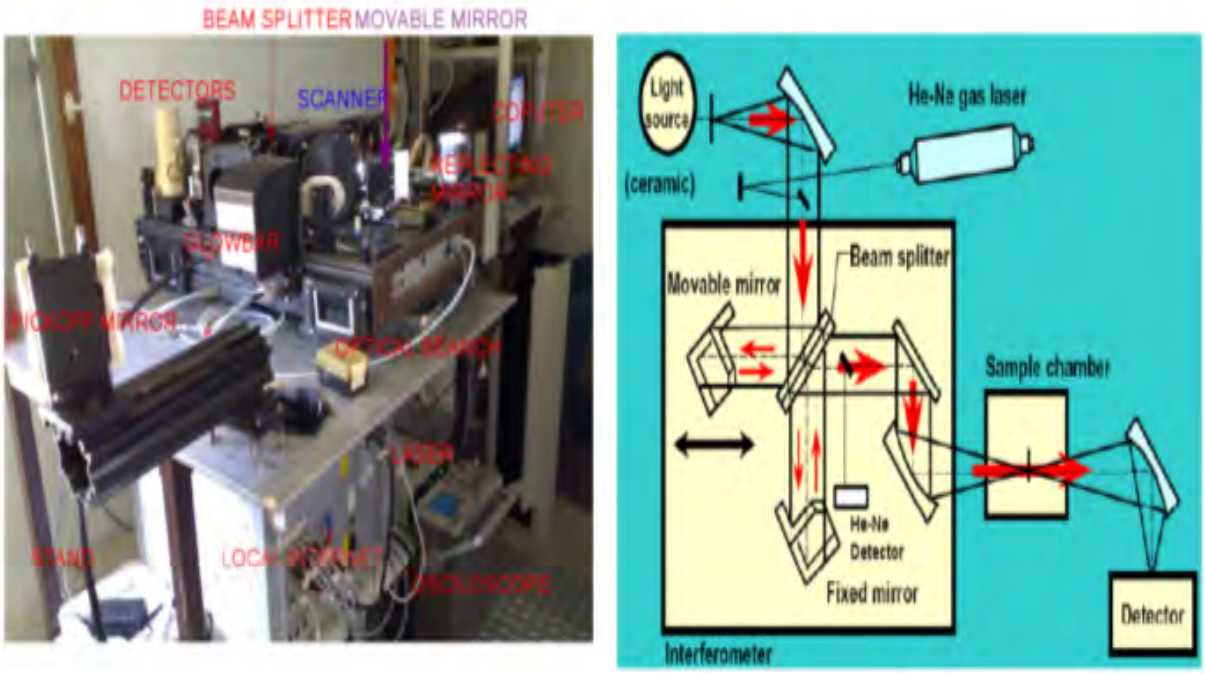

Figure 4.1: The FTIR Spectrometer [5].

FTIR is a technique of obtaining a spectrum such as

$$B(V) = \int_{-\infty}^{+\infty} I(\delta)\cos(2\pi V\delta)d\delta \tag{4.1.1}$$

from an interferogram such as

$$I(\delta) = \int_{-\infty}^{+\infty} B(V)\cos(2\pi\delta V)dV \tag{4.1.2}$$

using a mathematical operation known as Fourier transformation, where:

B (V) Is the intensity of the spectrum as a function of wave-number (V)

I(δ) is the interferogram (intensity versus time), and δ Is known as retardation or optical path difference [43].

4.1.2 Interference of Light

A monochromatic electromagnetic wave with an electric field strength E is given by

$$E = Ae^{i(k\cdot r-\omega t)}, \tag{4.1.3}$$

where A is the amplitude of the wave, k is the wave vector, r is the position vector, ω is the angular frequency and t is the time. In this expression

$$k = |k| = \frac{2\pi}{\lambda} = 2\pi\nu, \tag{4.1.4}$$

where λ is the wavelength of the electromagnetic wave. Both k and ν are called the wavenumber. It is convenient to express the wavenumber in the unit cm^{-1} instead of m^{-1} . Usually we are not able to measure E as a function of time, because the angular frequency, ω is too high. We measure the intensity, i.e., the power of the electromagnetic wave per area, instead. The intensity, I is proportional to the square of the amplitude:

$$I \propto A^2 \tag{4.1.5}$$

We examine the interference of two electromagnetic waves $E_1 = A_1e^{i(k_x\cdot x-\omega t)}$ and $E_2 = A_2e^{i(k_x\cdot x-\omega t+\delta)}$ propagating in the same direction x.

The waves, their amplitudes and the resultant amplitude are illustrated in Fig. 4.2. The phase difference of the two waves is δ. The square of the amplitude of the resulting wave is [5]

$$A^2 = A_1^2 + A_2^2 + 2A_1A_2cos\delta \tag{4.1.6}$$

If I_1 and I_2 are the intensities of the two interfering waves, the intensity of the interfered wave is

$$I = I_1 + I_2 + 2\sqrt{I_1I_2}cos\delta \tag{4.1.7}$$

If the two interfering waves have equal intensity, that is, $I_1 = I_2 = I_0$, then the intensity of the resulting wave is simply

$$I = 2I_0(1 + cos\delta) \tag{4.1.8}$$

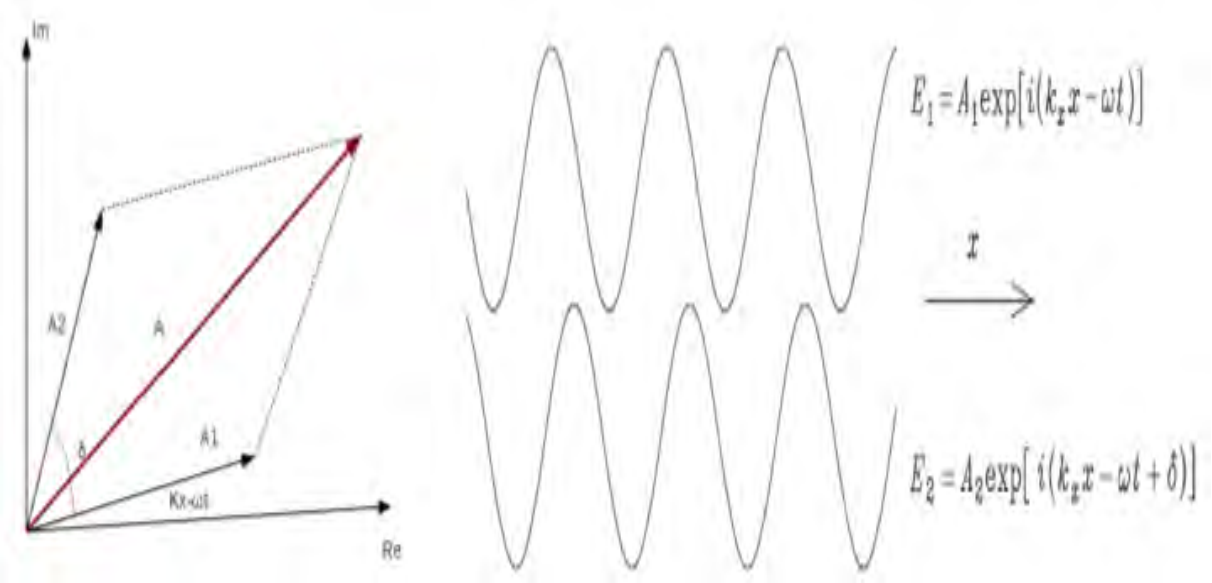

Figure 4.2: Interference of two waves E_1 and E_2. A is the resultant amplitude [5].

4.1.3 Michelson Interferometer

The design of many interferometers used for infrared spectrometry today is based on that of the two-beam interferometer originally designed by Michelson in 1891. Many other two-beam interferometers have subsequently been designed that may be more useful than the Michelson interferometer for certain specific applications. Nevertheless, the theory behind all scanning two-beam interferometers is similar, and the general theory of interferometry is most readily understood by first acquiring an understanding of the way in which a simple Michelson interferometer can be used for the measurement of infrared spectra.

The Michelson interferometer is a device that can divide a beam of radiation into two paths and then recombine the two beams after a path difference has been introduced. A condition is thereby created under which interference between the beams can occur. The variation of intensity of the beam emerging from the interferometer is measured as a function of path difference by a detector. The simplest form of the Michelson interferometer is shown in Fig. 4.3. It consists of two mutually perpendicular plane mirrors, one of which can move along an axis that is perpendicular to its plane.

Bisecting the fixed mirror and the movable mirror is a beamsplitter, where a collimated beam of radiation from an external source can be partially reflected to the fixed mirror (at point F for the median ray) and partially transmitted to the movable mirror (at point M). When the beams return to the beamsplitter, they interfere and are again partially reflected and partially transmitted. Because of the effect of interference, the intensity of each beam passing to the detector and returning to the source depends on the difference in path of the beams in the two arms of the interferometer. The variation in the intensity of the beams passing to the detector and returning to the source as a function of the path difference ultimately yields the spectral information in a Fourier transform spectrometer.

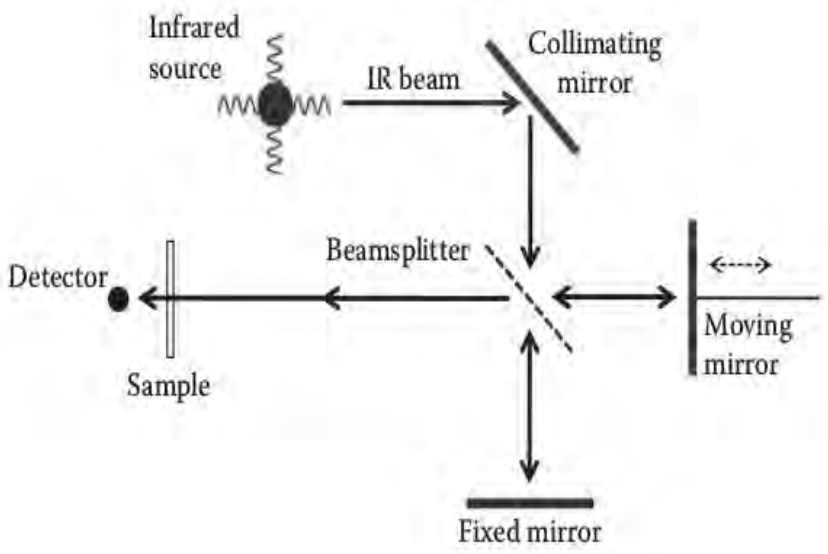

Figure 4.3: The optical diagram of a Michelson interferometer.

The beam that returns to the source is rarely of interest for spectrometry, and usually only the output beam traveling in the direction perpendicular to that of the input beam is measured. Nevertheless, it is important to remember that both of the output beams contain equivalent information. The main reason for measuring only one of the output beams is the difficulty of separating the output beam that returns to the source from the input beam. On rare occasions, both output beams are measured with the use of two detectors or by focusing both beams onto the same detector. In other measurements, separate beams can be passed into each arm of the interferometer and the resulting signal measured using one or two detectors. The movable mirror can either be moved at a constant velocity (a continuous scan interferometer) or be held at equally spaced points for fixed short periods and stepped rapidly between these points (a step-scan interferometer). When the mirror of a continuous-scan interferometer is moved at a velocity greater than $\sim 0.1cm \cdot s^{-1}$ (the usual case for most commercial instruments), the interferometer is often called a rapid-scan interferometer [44], [45].

4.1.4 Interferograms and Spectrum

An interferogram is the fundamental measurement obtained by an FTIR. Note that the shape of the interferogram in Fig. 4.4 is a cosine wave, and although it looks like a light wave, the interferogram is the electrical signal coming out of the detector. This is why the y-axis units in Fig. 4.4 are in voltage. Remember, we have made the simplifying assumption here that there is only one wavelength of light passing through the interferometer. Thus Fig. 4.4 represents the interferogram of a single wavelength of light. A laser gives off individual wavelengths of light, and so Fig. 4.4 represents the interferogram of a laser line [45].

An interferogram is obtained by varying the OPD (optical path difference) and recording the signal from the detector for various values of the OPD. It mesured from ZPD (zero

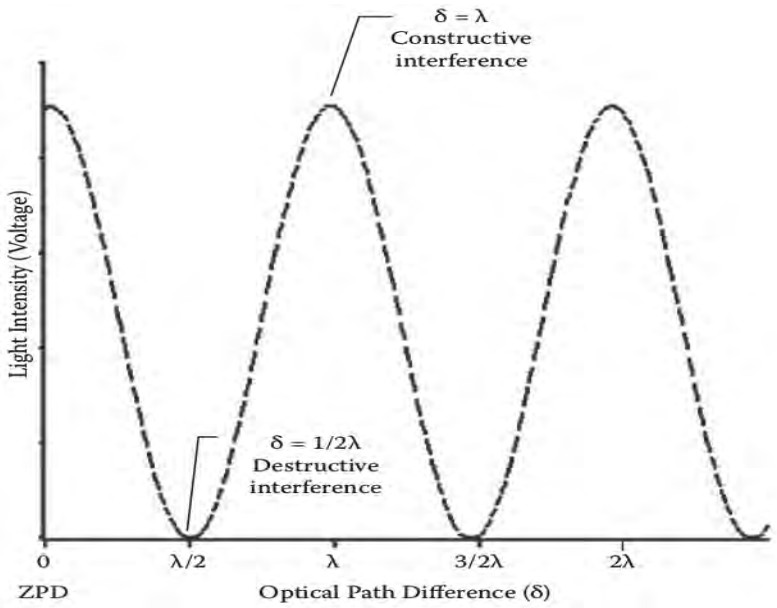

Figure 4.4: Light intensity (or detector signal) versus optical path difference for a mirror moving away from the beamsplitter in a Michelson interferometer. Such a plot is called an interferogram. This is the interferogram for a single wavelength of light passing through the interferometer.

path difference) to maximum length that depends on the resolution required because the interferograms is superposition of cosine wave, so that the Fourier transform of interferogram is a Spectrum. Spectrum is a plot of infrared intensity vs wavenumber (cm^{-1}).

4.1.5 The Sample Analysis Process of the FTIR

The normal instrumental process is as follows:

1. *The Source*: Infrared energy is emitted from a glowing black-body source. This beam passes through an aperture which controls the amount of energy presented to the sample (and, ultimately, to the detector).

2. *The Interferometer*: The beam enters the interferometer where the spectral encoding takes place. The resulting interferogram signal then exits the interferometer.

3. *The Sample*: The beam enters the sample compartment where it is transmitted

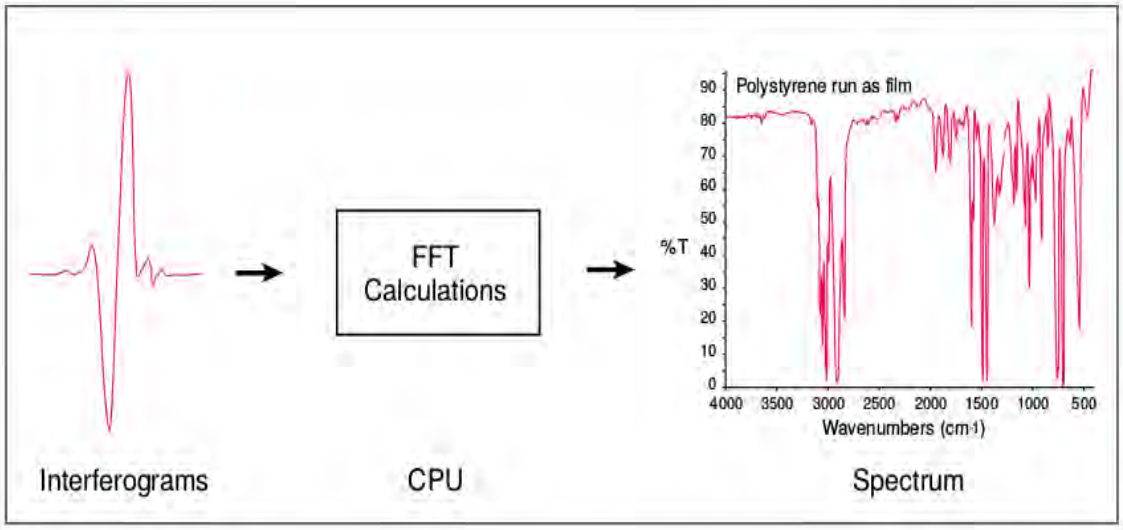

Figure 4.5: Interferograms is changed to Spectrum [46].

through or reflected off of the surface of the sample, depending on the type of analysis being accomplished. This is where specific frequencies of energy, which are uniquely characteristic of the sample, are absorbed.

4. *The Detector*: The beam finally passes to the detector for final measurement. The detectors used are specially designed to measure the special interferogram signal.

5. *The Computer*: The measured signal is digitized and sent to the computer where the Fourier transformation takes place. The final infrared spectrum is then presented to the user for interpretation and any further manipulation [46].

4.1.6 The FTIR Spectrometer and Retrieval

The BRUKER interferomenter is based on the IFS-120M model, but upgraded with the new electronics of the model IFS-125M. The FTIR spectrometer has two detectors: mercurycadmiumtelluride (HgCdTe) and indium antimonide (InSb), which allow coverage of the 600-1500 and 1500-4400 cm^{-1} spectral intervals, respectively. Recently, a new laser source with power supply has been mounted on this interferometer in order to

improve the laser signal that reaches the detector to attain stable movement of the optics. Typically, spectral resolution of 0.009 cm^{-1} is applied. FTIR spectrometer makes direct solar absorption measurements throughout the day, under clear sky conditions. The spectra are typically constructed by co-adding up to 10 scans recorded in about 8 min. A very large number of species of atmospheric relevance can be detected owing to its wide spectral coverage. In this paper, O_3 VMR profiles and column amounts are derived from measured spectra using version 9.5 of the retrieval code **PROFFIT** [48].

PROFFIT

PROFFIT was developed to analyse solar absorption spectra measured with high-resolution ground-based FTIR spectrometers; and it has been compared to other retrieval codes. Daily pressure and temperature profiles used in the retrievals are taken from the automailer system of Goddard Space Flight Centre [48]. The climatological profiles are based on data from the National Centre for Environment Prediction (NCEP) (http://www.cdc.noaa.gov/data/gridded/data.ncep.reanalysis.html). Spectroscopic data are taken from the High Resolution Transmission data (HITRAN) 2004 database. PROFFIT includes various retrieval options such as scaling of a priori profiles, the Tikhonov-Phillips method, or the optimal estimation method [49]. In this study, Tikhonov-Phillips regularization method is used during the retrieval. The retrieved state vector contains the retrieved logarithm of volume mixing ratios of the target gas defined in discrete levels in the atmosphere and retrieved interfering species column amounts, and fitted values for some model parameters. These include the baseline slope and instrumental line shape parameters. The retrieval of O_3 VMR profiles is performed on a logarithmic scale because O_3 concentrations around the tropopause are highly variable. Under these conditions a logarithmic scale inversion is superior to a linear inversion [48].

Line Fit

The knowledge of the instrumental line shape (ILS) is very important, otherwise wrong gas concentrations are deduced from the atmospheric measurements. LINEFIT which is a software that was developed by Hase to calculate and retrieve the instrumental line shape (ILS) using gas cell measurements. The description of retrieval procedure is that the user has to choose between either simple parameter set with a number of parameters $2+2n_w$, or extended parameter set with a number of parameters $40+2n_w, n_w$ denotes as spectral windows. Simple set and extended set are coupled by adjustable regularization constraint [43]. ILS gives an accurate knowledge about the spectral resolution over the measurements. The actual ILS of our IFS120M instrument is determined from low pressure gas cell measurement which is filled with HBr and radiation source of glow bar about at 1273K. Using the globar as a source of IR radiation, up to 100 scans are co-added to get spectra with and without the presence of an HBr cell placed in the parallel beam of a radiation source. The LINE FIT software was used to compute ILS by comparing the measured line shape with the theoretical one [5].

4.2 Methodology

The methods we used to study signature of tropospheric ozone over tropical africa are presented here.

In order to make sure that the line shape is reproduced correctly by the instrument, cell measurements are made and analyzed with LINE FIT Software. After knowing the ILS of our IFS120M instrument well. We are continued the collection of data from the atmosphere by adjusting the mirror on the solar tracker towards the sun position in order to reflect the light from the sun that has atmospheric information. The reflected sun light enters to the interferometer after processing in to the interferometer the detector gives the cosine-function form known as interferogram. Then the interferogram is Fourierlly transformed by OPUS (Optical user software) that are installed on the computer (is

component of the FTIR) and finaly we get a spectrum. Then the spectrum is as a function of frequency in order to change the spectrum in to computer understandably language (i.e to binary) we use OPUS software again for the calibration process in this stage the spectrum is changed in to DPT (Data point table) form.

In order to define the tropopause height , first the ECMWF temperature gridded data in the range of tropical Africa and using the FORTRAN code in [47] is downloaded.

We examined the OMI and MLS data record for evidence of high ozone and its precursor in the troposphere over tropical Africa. Finally back trajectories of air observed by FTIR are investigated. The HYSPLIT on line model is for back trajectory calculations. The HYSPLIT (Hybrid Single Particle Lagrangian Integrated Trajectory) model can give an idea of the history of the air parcel observed by FTIR.

Chapter 5

Analysis of Ground-Based Solar Absorption FTIR Spectra

The goal of FTIR experiment is to measure vertical profiles and column amount of TCO. To obtain these target quantities from measurement an inverse problem has to be solved. There exists various methods to solve such kind of problems. In most cases it is set up as a least square problem, where the different solution formula are quite similar. In this work different applications of both the optimal estimation (OE) and Tikhonov-Philips (TP) formalism are used as appropriate. The impact of constraints is shown under considerations of diagnostic tools such as retrieval error, vertical resolution and degrees of freedom [5].

5.1 Problem Description and Definitions

The retrieval problem in atmospheric remote sounding is to extract vertical profiles of atmospheric state parameters from sequence of absorption spectra of different heights. An exact physical description of the problem requires continuous functions. The vertical profiles to be retrieved are continuous functions with height while the spectrum is continuous function with frequency. Measurements are always discrete in nature. In this sense most of inverse problems are ill-posed [49]. To overcome this, the continuous functions of the vertical profiles are discretely sampled and arranged in a state vector $x \in R^n$ of unknown quantities whereby we will apply in the following the terminology used by

Rodgers [49]. This vector contains the finite number of unknown quantities which shall be determined in the retrieval. The width of the grid on which the atmospheric state parameters are represented depends both on practical considerations and on required altitude resolution. The m-dimensional measurement vector y contains all measured radiances to be considered for inversion. The measurement is superimposed by instrumental random noise. The correlation between the state vector x, the measurement vector y, the m-dimensional noise vector and the radiative transfer model F is given by

$$y = F(x) + \epsilon. \tag{5.1.1}$$

While the forward model maps from state space (vertical profiles) into measurement space (absorption spectra) we are interested in the inverse mapping, i.e., an appropriate determination of the state vector x from measurements. In our case the inverse problem is formally over-determined i.e, the number of measurements is higher than the number of state parameters ($m > n$). So the inverse problem can be formulated as least square problem.

$$\|y - F(x)\|^2 S_\epsilon^{-1} = [(y - F(x))]^T S_\epsilon^{-1}(y - F(x)), \tag{5.1.2}$$

where S_ϵ^{-1} is the covariance matrix of the measurement.

The nonlinearity of F(x) often requires Eq. (5.1.2) to be solved by Newtonian iteration [50].

$$x_{i+1} = x_i + (K_i^T S^{-1} K_i)^{-1} K_i^T S_{-1}(y - F(x_i)), \tag{5.1.3}$$

where K is the Jacobian of F with respect to x and the subscript i denotes the iteration index. This solution uses information only from the measurement. Additional information about the solution can be included by including a constraining term. This can be a climatology derived from set of independent measurements of the atmospheric constituents to be retrieved.

$$\|y - F(x)\|^2_{S_\epsilon^{-1}} + R(x, x_a, R) = [(y - F(x)]^T S_{-1}(y - F(x)) + (x - x_a)^T R(x - x_a), \tag{5.1.4}$$

where R is the constraining function [51], x_a is an a priori known state vector and R is a regularization matrix. The resulting iterative solution is then given by

$$x_{i+1} = x_i + (K_i^T S^{-1} K_i + R)^{-1}[K_i^T S^{-1}(y - F(x_i)) - R(x_i - x_a)], \tag{5.1.5}$$

where x is the retrieval vector, K, the partial derivatives of the spectra with respect to the retrieval vector (Jacobian) , S the covariance matrix due to measurement noise, R, the regularization or constraint matrix, y, measurement vector, F, the forward model, x_a the a priori profile and i the iteration index.

Based on the choice of the regularization matrix, different kinds of constraints can be included in the least squares problem.

5.2 Retrieval Strategy

The iterative solution given by Eq. (5.1.5) can be seen as a weighted mean of the information contained in the measurement and the information added by the constraint. Determination of the appropriate weight of the constraint is a critical part of the design of any retrieval strategy. Different kinds of constraints can be implemented to solve inverse problems such as optimal estimation (OE) and Tikhonov regularization. In case of optimal estimation the difference between the a priori profile x_a and the solution is kept small. The regularization matrix is $R = S_a^{-1}$ the inverse of the a priori matrix, and the iterative solution is

$$x_{i+1} = x_i + (K_i^T S^{-1} K_i + S_a^{-1})^{-1}[K_i^T S^{-1}(y - F(x_i)) - S_a^{-1}(x_i - x_a)]. \tag{5.2.1}$$

When the inverse of the covariance matrix for the measured profile $K^T S_\varepsilon^{-1} K$ larger entries than the inverse of a priori covariance matrix S_a^{-1} the retrieval is dominated by the measurement with its noise. If the a priori information comes from an independent measurement or if x is part of a climatological ensemble, following Gaussian statistics which is represented by x_a and S_a the optimal estimation is the most probable solution

[49]. However, if there is no independent measurement, which provides x_a and if x is not part of the statistical ensemble which is represented by x_a and S_a the result is to some degree biased towards the a priori profile. A solution constrained in its shape only rather than in its absolute value may be more desirable in order not to miss unexpected atmospheric phenomena. For this purpose Tikhonov regularization is a powerful tool. In case of Tikhonov regularization the matrix becomes $R = \alpha L^T L$, where α is a regularization parameter and L is a regularization matrix. This kind of regularization is also known as Twomey or Philips regularization [51] and the iterative solution is given by

$$x_{i+1} = x_i + (K_i^T S^{-1} K_i + \alpha L^T L)^{-1}[K_i^T S^{-1}(y - F(x_i)) - \alpha L^T L(x_i - x_a)]. \qquad (5.2.2)$$

The parameter α determines the weight of the regularization and it is also important to choose α appropriate to the problem. One way to fix this parameter is the L-curve method [52]. There are several possibilities to set up regularization matrix L, the simplest one being the identity matrix, I = L. This results in a retrieval equivalent to the optimal estimation with a diagonal a priori covariance matrix $S_a = \frac{1}{\alpha} I$. In order to obtain a smooth solution the discrete first derivative operator is useful as a smoothing matrix, $L = L_1$. The discrete first derivative operator can be derived as follows: the first derivative can be approximated as

$$x_k^{'} \approx \frac{x_k - x_{k-1}}{z_k - z_{k-1}}, \qquad (5.2.3)$$

where x_k is the state parameter at height z_k .

By approximation of the first derivative by a differential quotient and in case of equiv-

alent altitude grid the operator is defined as

$$\begin{pmatrix} X^{2'} \\ . \\ . \\ . \\ X^{n'} \end{pmatrix} \approx \begin{pmatrix} -1 & 1 & 0 & . & . & . & 0 \\ 0 & -1 & 1 & . & . & . & . \\ . & . & . & . & . & . & . \\ . & . & . & . & . & . & . \\ . & . & . & . & . & . & 0 \\ 0 & . & . & . & 0 & -1 & 1 \end{pmatrix} = \begin{pmatrix} X^1 \\ . \\ . \\ . \\ X^n \end{pmatrix} = L_1 X \tag{5.2.4}$$

This and higher order kind of operator act just in smoothing not biasing the solution. In the case that two different types of state parameters being jointly fitted, which require different approaches of regularizations, it is necessary to have one formalism which supports both types of constraints. In order to gain understanding of the smoothing effect of the off-diagonal elements of S_a , we to express $\alpha L_1^T L_1$ by a matrix of the format of an inverse covariance matrix as[51]

$$S_a^{-1} = \alpha L_1^T L_1 \tag{5.2.5}$$

This means that an a priori covariance matrix can be set up that acts approximately in the same way as the discrete first derivative operator L_1. This equivalence is only approximate since truncation of the expansion causes a regular matrix S_a^{-1} being transformed to a singular matrix of the form $L_1^T L_1$. Therefore optimal estimation formalism can be used either in the original sense of weighting the measured and the a priori profile or in the sense of smoothing the solution without considerably shifting it towards the a priori profile. Because of the approximate equivalence of OE and TP regularization methods, we henceforth use the optimal estimation terminology.

5.3 Diagnostics

Following Rodgers [49] a number of diagnostic tools are available and will be used for assessment of the retrieval. These include: covariance matrix of the retrieved solution, averaging kernel matrix and degrees of freedom. The covariance matrix of the solution

includes the estimated error of the state parameters and their inter-level correlations:

$$\hat{S} = (K^T S_\epsilon^{-1} K + S_a^{-1})^{-1} \tag{5.3.1}$$

Another important quantity to assess the retrieval is the vertical resolution. The vertical resolution depends on the sensitivity of the retrieval to changes in the true profile:

$$A = \frac{\partial \hat{X}}{\partial X} = D_y K \tag{5.3.2}$$

where $\hat{X}$ is the estimated profile in the linear case and D_y describes the sensitivity of the retrieval concerning changes in the measurement:

$$D_y = \frac{\partial \hat{X}}{\partial y} \tag{5.3.3}$$

The matrix A is usually called the averaging kernel matrix. There are several ways to define the vertical resolution of the retrieval as a function of A [53]. We define the vertical resolution as the width at the half maximum of the column of the averaging kernel matrix. The averaging kernel matrix for the optimal estimation is calculated as

$$A = (K^T S_\epsilon^{-1} K + S_a^{-1})^{-1} K^T S_\epsilon K \tag{5.3.4}$$

If there is no constraining term in the least square problem (Eq.(5.1.2)), the averaging kernel matrix is the identity matrix I. In this case the altitude resolution is determined by the grid used for representation of x. The estimated solution for optimal estimation can also be expressed in terms of the averaging kernel. In the linear case the gained equation allows to separate the true parameters and the apriori parameter. The estimated solution is

$$\begin{aligned} \hat{X} &= X_a + A(X - X_a) + D_y \epsilon \\ \hat{X} &= AX + (I - A)X_a = D_y \epsilon \end{aligned} \tag{5.3.5}$$

where the averaging kernel A is the weight of the true state, the matrix (I - A) is the weight of the true a priori state and D_y the weight of the noise. In case of no constraints

(I = A), the a priori part of (Eq. (5.3.5)) disappears and the result depends only on the true state and the noise. Because the matrices of the weights A, (I - A) and D_y are usually non diagonal, it is not trivial to quantify the different parts of the retrieval formula (Eq. (5.3.5)). A transformation in space where the matrices described above become diagonal is proposed by Rodgers [49]. For this purpose the Jacobian K has to be transformed and a singular value decomposition (SVD) is performed [54]:

$$\tilde{K} = S_\epsilon^{-\frac{1}{2}} \tilde{K} S_a^{\frac{1}{2}} = U \Lambda V^T \tag{5.3.6}$$

where U and V are orthogonal matrices and Λ is a diagonal matrix with the singular values λ_i of $\tilde{K}$ as its diagonal elements. Moreover U is m×n matrix, V and Λ are n×n matrices. The state vector and the noise vector are transformed as follows

$$\begin{aligned} X^{'} &= V^T S_a^{-\frac{1}{2}} X \\ \epsilon^{'} &= U^T S_\epsilon^{-\frac{1}{2}} \epsilon \end{aligned} \tag{5.3.7}$$

with the singular value decomposition of $\tilde{K}$ (Eqs. (5.3.6) and (5.3.7)) we get for the transformed estimated state parameters

$$\hat{X}^{'} = [I + \Lambda^2]^{-1} \Lambda^2 X^{'} + [I + \Lambda^2]^{-1} X_a^{'} + [I + \Lambda^2]^{-1} \Lambda \epsilon^{'} \tag{5.3.8}$$

The matrices in the different addends are diagonal now. So (Eq.(5.3.8)) can be written component wise as

$$\hat{X}_i^{'} = \frac{\lambda_i^2}{1 + \lambda_i^2} X_i^{'} + \frac{1}{1 + \lambda_i^2} X_{ai}^{'} + \frac{\lambda_i}{1 + \lambda_i^2} \epsilon_i^{'} \tag{5.3.9}$$

We can see from Eq. (5.3.9) that the transformed state parameter $\hat{X}_i^{'}$ is dominated by the true profile if the corresponding singular value is much larger than 1 ($\lambda_i \gg 1$). For cases $\lambda_i \ll 1$, the corresponding state parameter is determined by the priori knowledge. For singular values $\lambda_i \approx 1$, the estimated state parameter is influenced by the true state, the a priori state and the noise with the same weight. (Eq.(5.3.9)) leads to the definition of the degrees of freedom for signal [49]:

$$d_s = \sum_i \frac{\lambda_i^2}{1 + \lambda_i^2} \tag{5.3.10}$$

The singular values with $\lambda_i \ll 1$ do not contribute to the degrees of freedom because they will be determined by the a priori knowledge. Therefore the number of degrees of freedom is not fixed with the dimension of the state space n but rather with the quantity computed within Eq. (5.3.10). The diagnostic tools where the singular value decomposition of the transformed Jacobian is used is for the special application to the optimal estimation formalism.

5.4 Error Estimation

Any error modifies the spectrum, thereby disturbs the retrieved quantities. This section provides a brief description of the error estimation, which includes measurement, smoothing and interfering species error.

The error estimation assumes that, we are in an incrementally linear regime.

$$X_{est} = X_a + G\epsilon + A(X_{true} - X_a) + GK_b(b_{true} - b_{est}) \tag{5.4.1}$$

where A is the averaging kernel, X_a is the a priori constraint vector, X_{true} is the true state, G is the gain matrix, ϵ is the measurement error, K_b is the Jacobian matrix of the interfering species and b is the state of the interfering species. A and G are calculated from the Jacobian of the retrieved species, the constraint matrix and the estimated radiance errors.

The estimated error covariance is defined as

$$S_{err} = \langle (X_{est} - X_{true})(X_{est} - X_{true})^T \rangle \tag{5.4.2}$$

This error covariance can be calculated using Eq. (5.4.1)

$$S_{err} = \underbrace{(1-A)S_a(1-A)^T}_{smoothing} + \underbrace{GS_mG^T}_{measurement} + \underbrace{GK_bS_b(GK)^T}_{systematic} \tag{5.4.3}$$

where S_a is the a priori covariance of the retrieved state, i.e, $\langle (X_{est} - X_{true})(X_{est} - X_{true})^T \rangle$ S_m is the measurement error covariance and S_b is the error covariance of the interfering

species. The square root diagonal of Eq. (5.4.3) gives error bars commonly reported and the various terms are helpful to determine the sizes of the various error components.

Chapter 6

Results and Discussion

Since May 2009, high-resolution Fourier Transform Infrared (FTIR) solar absorption spectra have been recorded at Addis Ababa (9.01^0N latitude, 38.76^0E longitude, 2443 m altitude above sea level). FTIR solar absorption spectra are recorded under clear-sky conditions, 8 to 10 minute constructed by co-adding up to 10 scans.

Analysis of the results obtained after employing a scheme in chapter five is discussed in detail. We present the detail results in this chapter.

6.1 Spectral Line Fit

The mean of error is -2.2818×10^{-07}, the minimum and maximum error deviation is -0.0070 and 0.0079 respectively so the fluctuation range is between (-0.0079 and 0.0070)(see Fig. 6a-b). The Modulation efficiency and phase error during the measurement time (Fig 6.1 c - d) is clearly show that the modulation efficiency nearly constant with minor variation around 100% to 100.0011%. The phase error also fluctuates to $\pm$ 0.0003 rad.

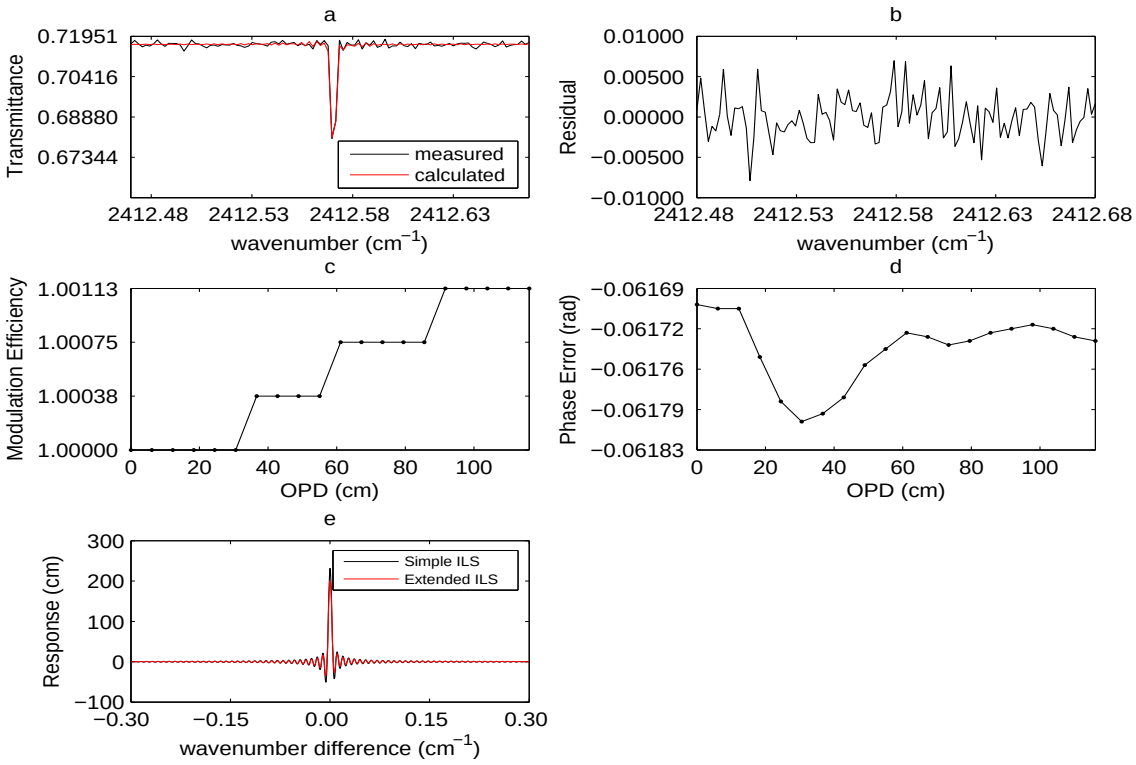

Figure 6.1: The measured and simulated transmittance spectral fit from HBr cell measurement (a), the corresponding residual spectra between the measured and calculated spectra (b), Modulation efficiency and Phase error with OPD (c and d respectively) and the Response that show simple and extended ILS at the legend (e) on the Measurement dates Dec/21/2015.

6.2 ozone Spectral Signature in the Mid-Infrared

6.2.1 Spectral Regions

For the retrieval 4 optimum spectral regions (micro windows) have been used between 3041.480000 cm^{-1} and 3045.550000 cm^{-1}. Because ozone is highly sensitivity to this spectral regions and there is only low interference by other gases. However, the contribution of other gases still needs to be considered even after careful micro window selection. These interfering gases are H_2O and CH_4 . The retrieval procedure follows a scheme described by Eq. (5.1.5). The retrieval is performed on a fine vertical grids from $2 \cdot 45$ to 85km and is stabilized by a first order Tikhonov constraint described by Eq (5.2.2) which smooths the solution without biasing it towards the a priori profile.

Table 6.1: List of micro windows used for ozone inversion. For each of them the interfering species adjusted during the retrieval procedure are included.

Micro window bounds (cm^{-1})	Target gas	Interfering species
3041.480000 - 3041.940000	O_3	H_2O and CH_4
3042.930000 - 3043.240000	O_3	H_2O and CH_4
3044.250000 - 3044.620000	O_3	H_2O and CH_4
3045.260000 - 3045.550000	O_3	H_2O and CH_4

The code to simulate the observed spectrum calculates the radiative transfer equation iteratively through 41-layer atmosphere. Following this calculation the radiance is convolved with the FTIR instrument line shape and then apodized with boxcar medium apodization. Each retrieval step minimizes a cost function (Eq. 5.1.2) using a Tikhonov-Philips (TP) nonlinear least square algorithm [PROFFIT (V9.5)] where the cost function chosen considers both spectroscopic fit over the spectral windows used and our a priori knowledge of the atmosphere. The spectral windows are selected to maximize the information content of a retrieval given an expected a priori covariance. The ozone a priori profiles are created from tropical climatology and combined into a single profile using interpolation. Four of the spectral regions (micro windows) used in this study to retrieve the target gas (O_3) together with the fitted species are displayed in Fig. 6.2.

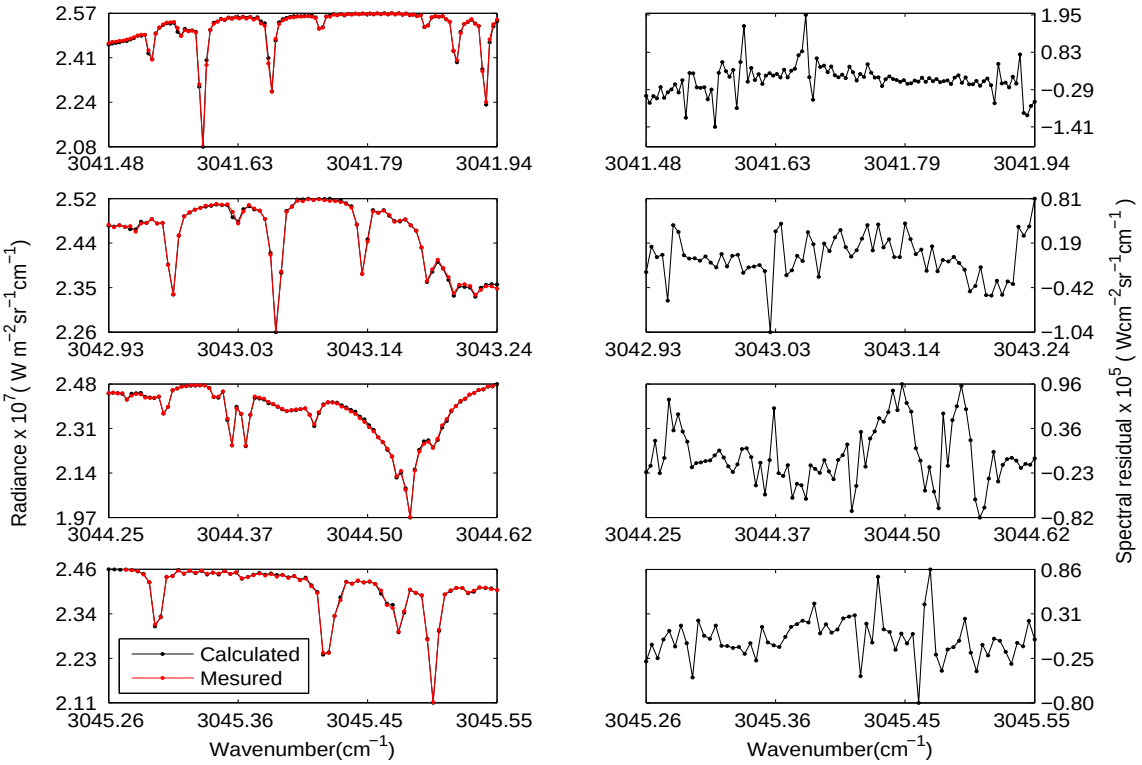

Figure 6.2: Multiple micro-window fit of O_3 and interfering species. Measured (red) calculated (black) spectra are shown (left plots) together with residuals (right plots).

All settings (micro-windows, constraint, initial guess and a priori profile) are chosen in such a way that all the structures visible in the retrieved distributions originate from the measurements and are not artifacts due to any constraints. The retrieved result of the experiment is displayed in Table 6.2.

Table 6.2: Ozone (O_3) retrieval results and uncertainties for some selected altitudes.

altitude(km)	2.45	2.94	3.556	4.208	4.896	5.620	17.12	18.31	19.54
a priori(ppmv)	0.047	0.048	0.051	0.054	0.056	0.059	0.168	0.380	0.888
retrieved(ppmv)	0.025	0.026	0.027	0.028	0.029	0.029	0.247	0.452	0.771
uncertainty(%)	0.021	0.023	0.024	0.026	0.028	0.030	0.079	0.073	0.117

6.2.2 Single Profile Retrieval of Ozone and Diagnostics

The retrieval procedure described in the previous chapter has been applied to real FTIR measurements. Fig. 6.3 shows a single profile retrieval of O_3 for on 21-12-2015 at Addis Ababa.

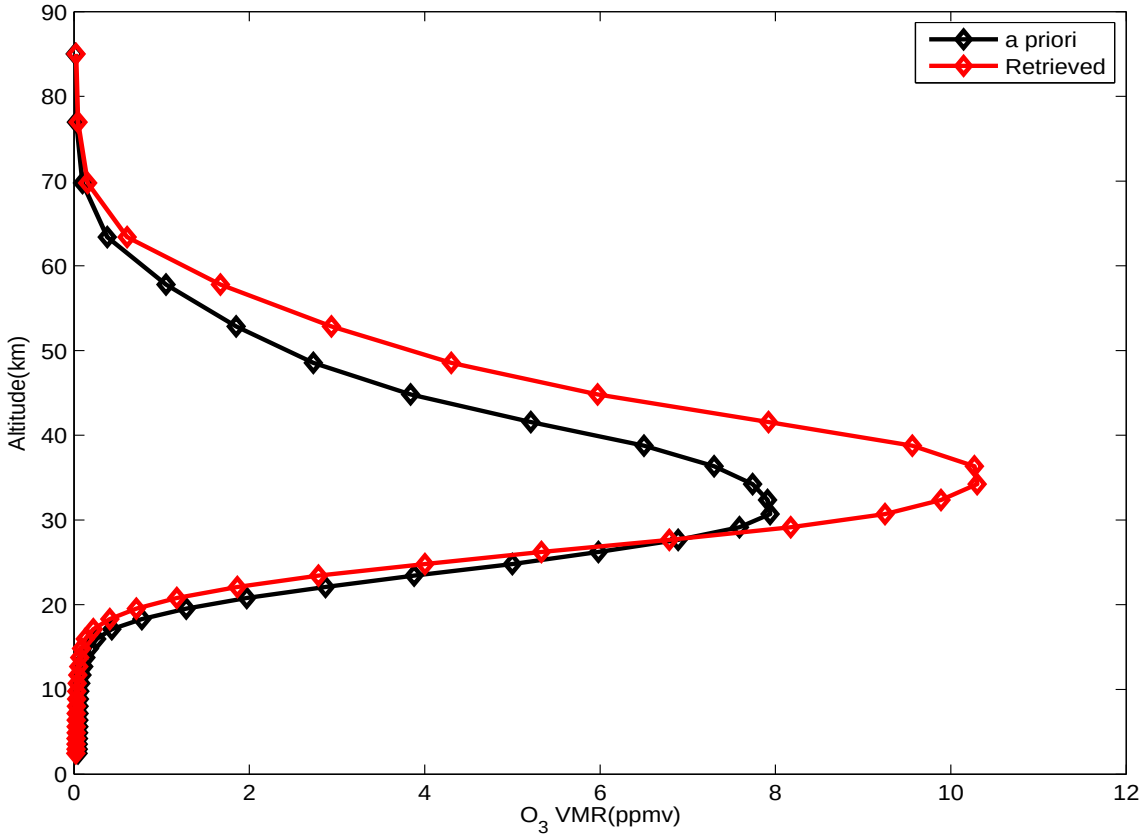

Figure 6.3: Vertical profile of ozone (O_3) retrieval result (FTIR,21-12-15,9.01^0N,38.76^0E).

The maximum difference is observed in the stratosphere around (34.23 to 41.57) km.This maximum difference at this altitudes 3.06 ppmv.The maximum value of retrieved VMR (10.3000 ppmv) is found in the stratosphere and the minimum value (0.0220 ppmv) is found in lower troposphere.

6.2.3 Vertical Information in Retrievals from FTIR Spectra

The vertical information contained in the retrievals can be characterized by the averaging kernel matrix in Eq (5.3.2). This matrix depends on measurement and retrieval parameters including the SZA, the spectral resolution and signal to noise ratio, the choice of spectral micro windows, and the a priori covariance matrix. Figs. 6.4 show the rows of the averaging kernels matrix for a typical profile retrieval of O_3 on the 41-layer height grid. They indicate at each altitude the fraction of the retrieval that comes from the measurement rather than from the a priori information. A value of zero and near to zero at a certain altitude indicates that the retrieved profile at that altitude is nearly independent of the real profile and is therefore approaching the a priori profile. So the integrated area under each averaging kernel is a simple measure of the amount of non a priori information that appears in the retrieval at the corresponding height. The figure shows clearly the retrieval is most sensitive in stratosphere.

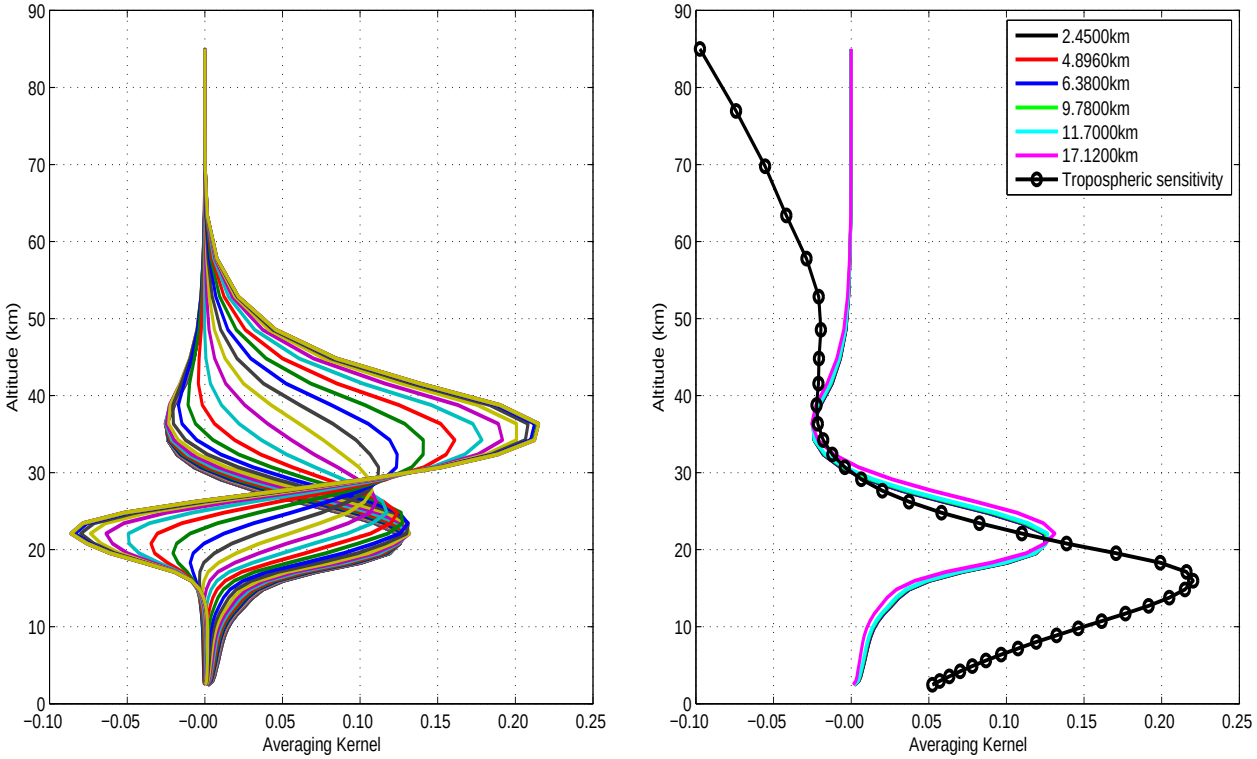

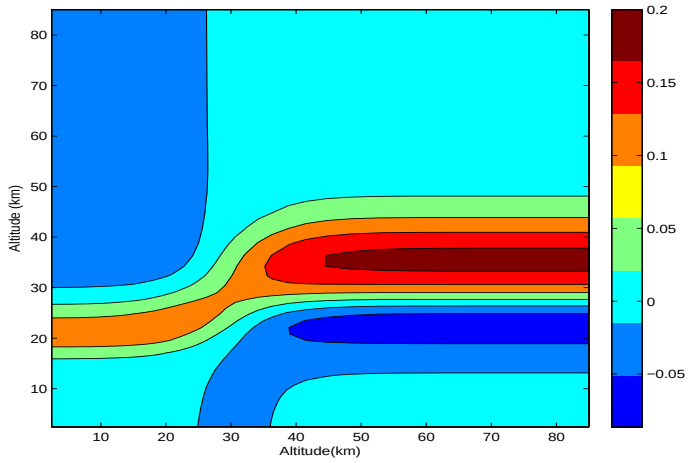

Figure 6.4: (First panel) Averaging kernel of (O_3) for all layer (Medial panel) Averaging kernel for some selected heights and (third panel) It shows where the information is coming at a given height.

6.3 Tropopause Height over Tropical Africa

The pressure at the tropopause varies on average between 90hpa to 105hpa

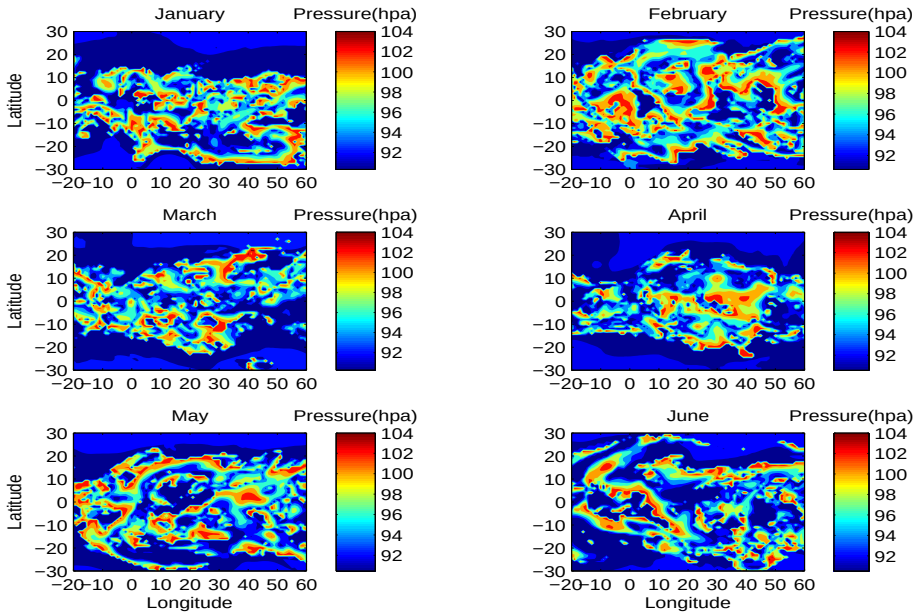

Figure 6.5: Mean characteristics of the tropopause pressure Variation range (2010).

6.4 TCO Time Series Analysis

Fig. 6.6 shows a comparison between the FTIR observation and the OMI/Aura satellite. The maximum TCO of the satellite does not exceed $1.2 \times 10^{18} molecule/cm^2$. In contrast to the satellite observation, the FTIR observation exceeds this value during some cases. Statistical analysis of the enhanced periods clearly indicated that those enhanced measurement in May 2009 were removed from the data set for they are outliers. The remaining two measurements occurred in January 2011 identified as enhancement of the tropospheric ozone of the respective days. The cause of the increased column values is left for later discussion.

The tropospheric ozone obtained from the satellite is the difference between the total column of the OMI/Aura with the stratospheric column obtained from MLS/Aura. The ozone measurements from the ground observing system is then compared to that of the satellite. The statistical characteristic of the tropospheric ozone from the two observing systems with their difference is given in Table 6.3. Accordingly, the mean relative difference of the FTIR data are 18.1% with OMI-MLS.

Table 6.3: Comparison of TCO ($\times 10^{17} molecule/cm^2$) from FTIR and satellite.

Device	Minimum	Maximum	RMS	Mean	STD
FTIR	3.2551	13.0080	8.0262	7.8597	1.6299
OMI-MLS	6.0694	12.6340	9.3563	9.2826	1.1734
FTIR-(OMI-MLS)	-0.5553	3.3240	0.2361	-0.1394	0.1914

The minimum TCO of the FTIR occurred in May 22, 2009, and the maximum on January 17, 2011. While the satellite measurements showed the minimum and maximum TCO Values in Feb 20, 2015 and January 15, 2015 respectively.

The lower panel of Fig. 6.6 suggest that there is considerable data difference between the FTIR and the OMI-MLS measurements. A possible explanation is that there is

a difference in the technique of measurement of the observing systems. That is the FTIR uses IR spectra while the OMI uses UV. In addition, indirect measurement of the tropospheric ozone column may be subjected to two possible source of error: during the measurement of the total column by the OMI and the stratospheric column by MLS. In taking the difference of the two may result in an increased uncertainty of the result.

Inter-annual comparison of TCO shows that, there is a slight variation of the column amount among the years. Despite limited number of FTIR observations and short record length, there is a slight indication of positive trends towards 2015. This is further strengthened by the satellite measurement. The summary of statistical analysis of comparison is given in Table 6.4.

Table 6.4: Statistical analysis of TCO ($\times 10^{17} molecule/cm^2$) of the year .

Year	Minimum	Maximum	RMS	STD	Mean
2009	3.2551	11.0230	7.9359	1.8111	7.7366
2010	5.5667	8.0311	6.5931	0.5750	6.5686
2011	9.6256	13.0080	10.7220	0.8640	10.6890
2012	5.6762	6.85850	6.2418	0.3218	6.2338
2013	5.6601	6.8677	6.2629	0.2795	6.2569
2014	7.8083	10.0860	9.0662	0.50390	9.0530
2015	5.8746	10.8350	8.9745	0.9247	8.9273

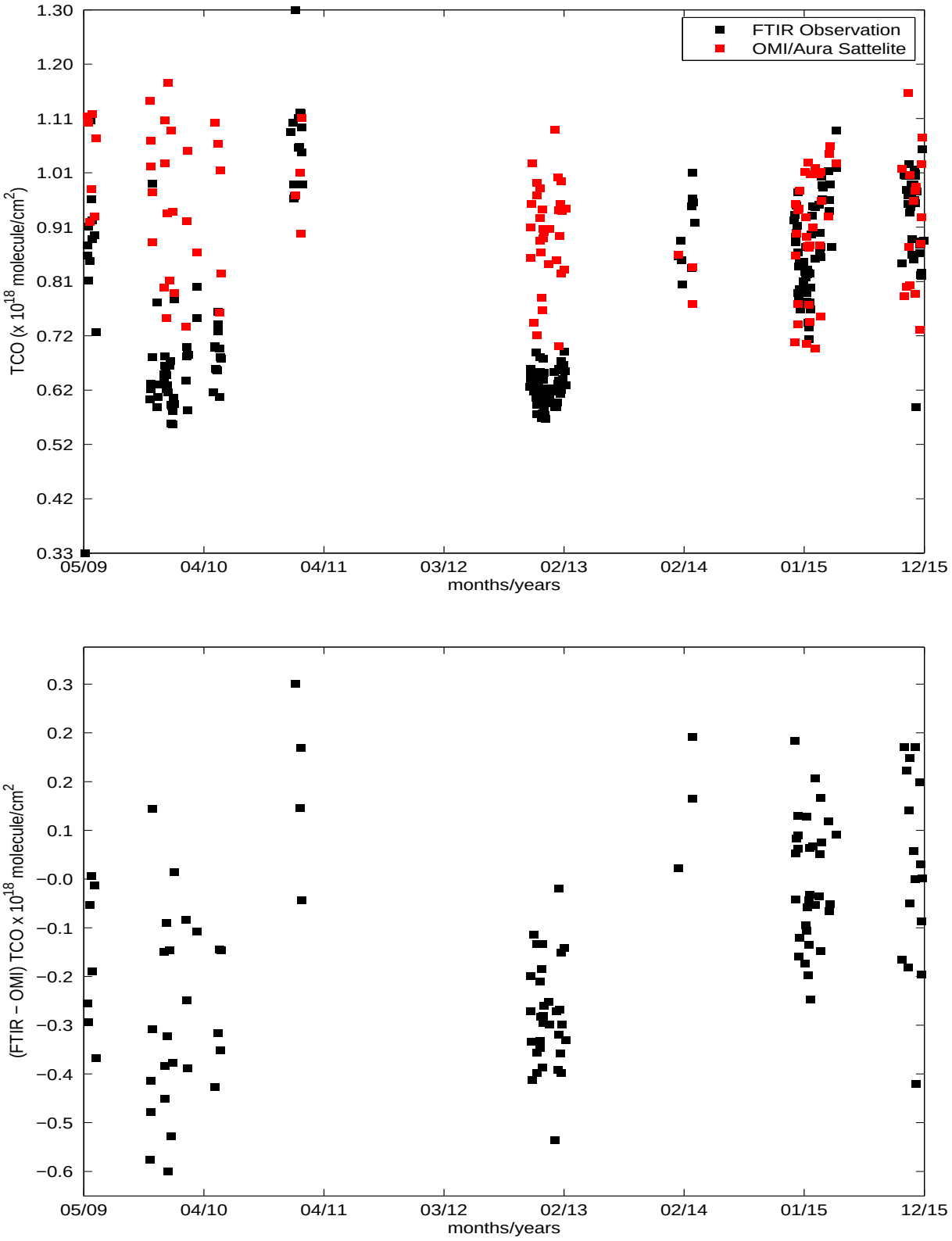

Figure 6.6: Upper panel Time series of TCO Comparison among FTIR and OMI Lower panel The difference between FTIR and OMI of the year (may 2009 to Dec 2015).

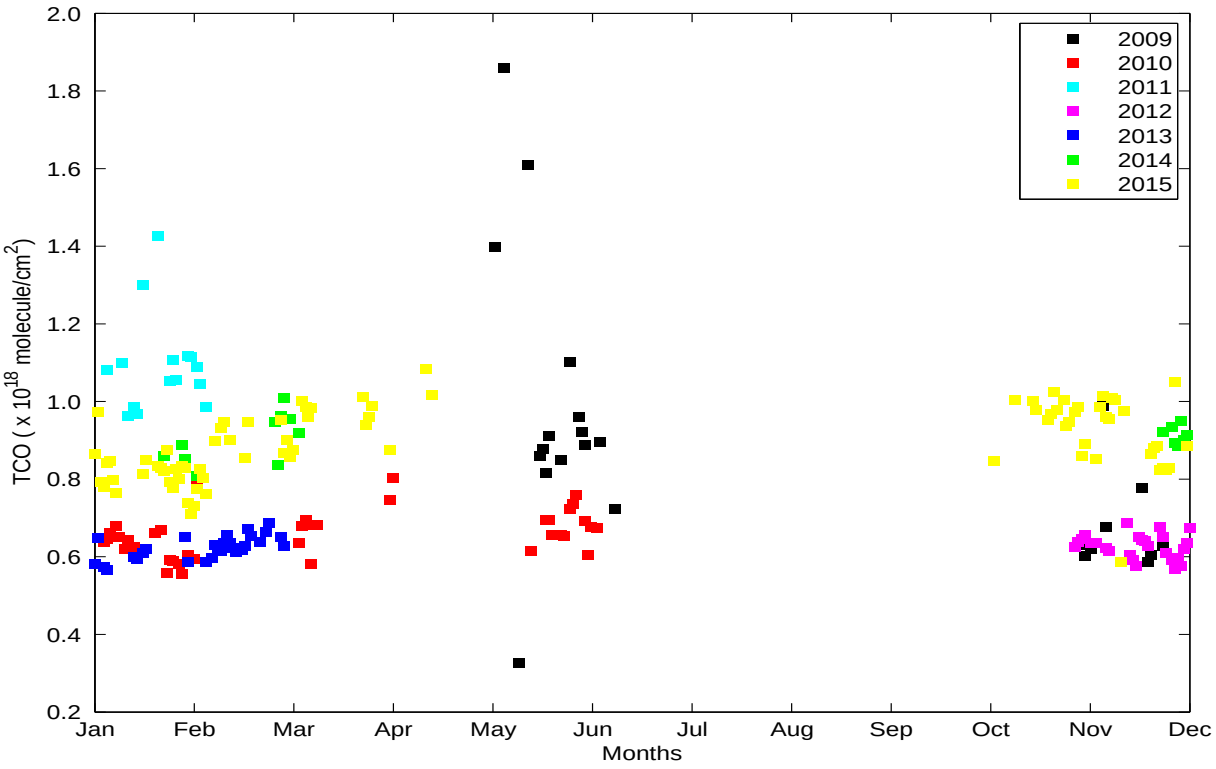

Figure 6.7: TCO between 2009 to 2015 from FTIR observation

6.5 Treatment of the Enhanced Periods

The main source of ozone in the troposphere are due to its precursors and the stratosphere-troposphere exchange. Among the precursors of O_3, CO and NO_2 are the trace gases responsible for O_3 production and destruction. The main source of CO in Africa is biomass burning areas such as savanna, forest fires, etc. In addition,the high abundance or absence of NO_2 is an indicator of high or low level production of O_3. MOPITT satellite data to check the concentration of CO of May 22, 2009 and January 17, 2011. Moreover, the age of the air reaching the FTIR observation site is important to locate the potential source region. Thus, the fire map from CMAS fire Assimilation and the NO_2 of the three days obtained from OMI satellite data are used (See Figs. 6.8-6.10). HYSPLIT back trajectory is also employed to determine the source direction and determine consistency between different data sets.

Fig. 6.8 indicates that there is uninterrupted release of carbon flux in the latitude between 0°and 10°N. This region is nearest to the equatorial belt known by biomass burning. MOPITT also strengthened evidence for the presence of greater CO column amount near the equatorial Africa, $\sim 40 \times 10^18 molecule/cm^2$. In addition, the VMR of CO is between 45-65ppbv (see Fig. 6.9) with in the troposphere. The contour maps in Fig. 6.10 The accumulated NO_2 reaching $18 \times 10^{15} molecule/cm^2$ has been detected to the west of the observation site.

Trajectory of air mass calculation in Fig. 6.12 shows that the South-West and North-East of the FTIR site were important sources of the precursors of ozone.

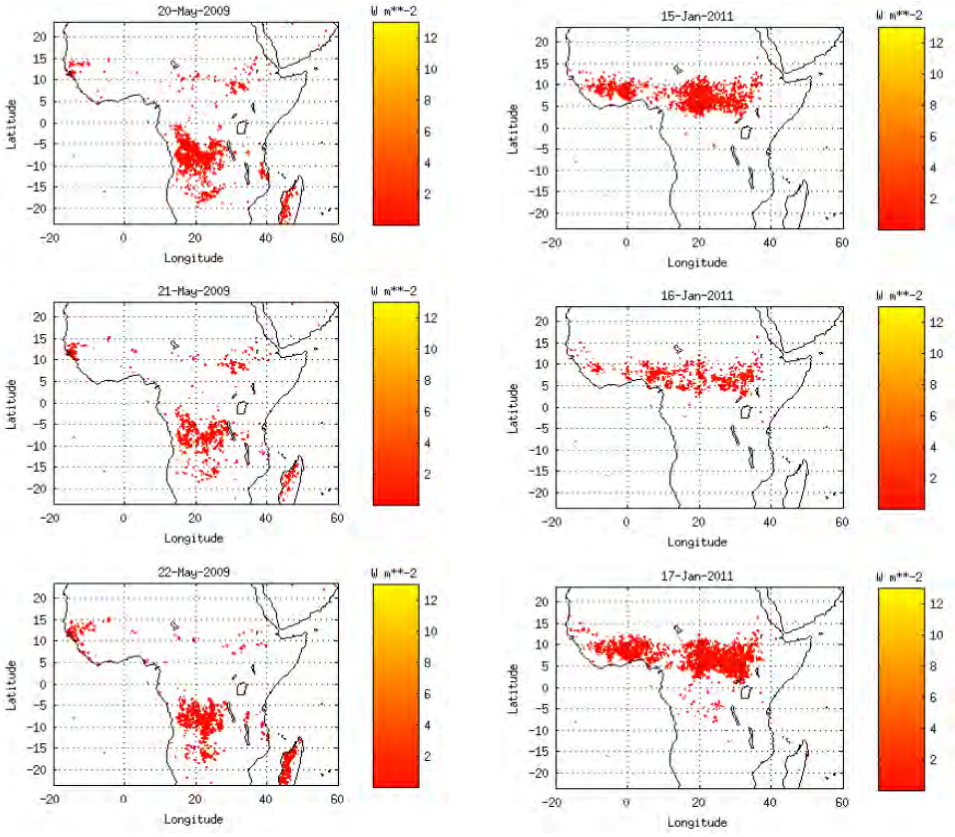

Figure 6.8: Biomass burning areas during the period shown on each panel (CAMS GlobalFire Assimilation system (GFASv1.0) from ECMWF data sets).

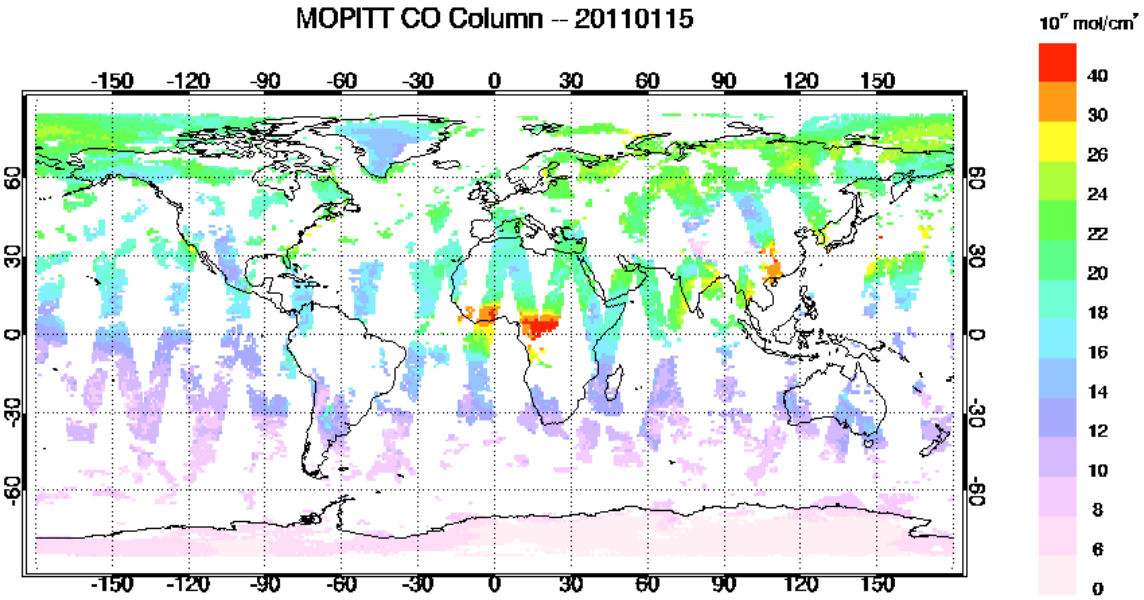
MOPITT CO Column -- 20110115
10^18 mol/cm^2
40
30
26
24
22
20
18
16
14
12
10
8
6
0
-150 -120 -90 -60 -30 0 30 60 90 120 150
60
30
0
-30
-60

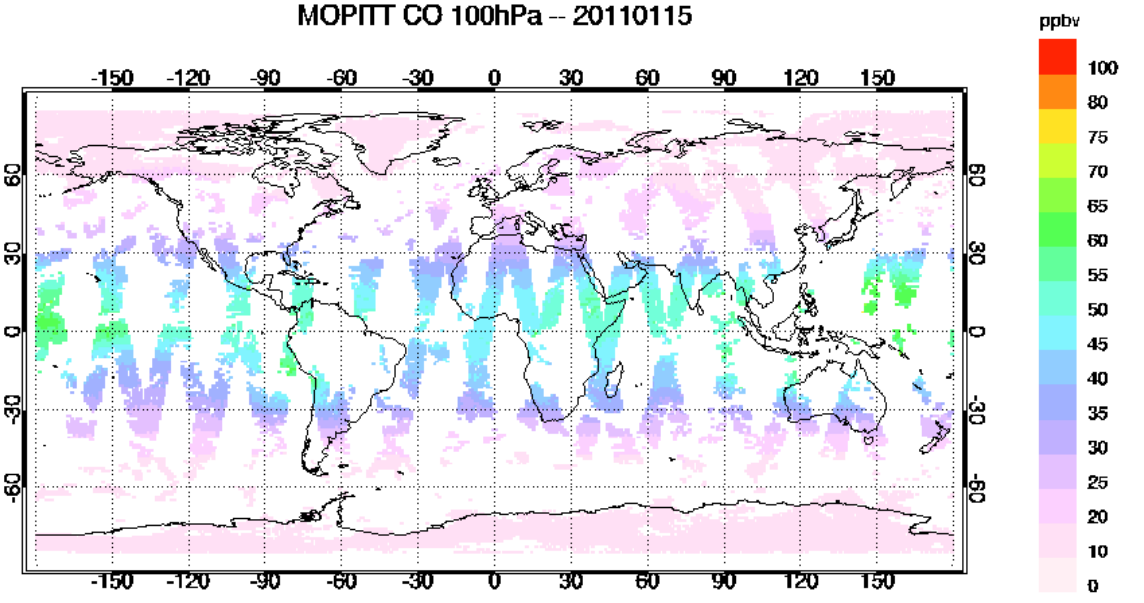
MOPITT CO 100hPa -- 20110115
ppbv
100
80
75
70
65
60
55
50
45
40
35
30
25
20
10
0
-150 -120 -90 -60 -30 0 30 60 90 120 150
60
30
0
-30
-60

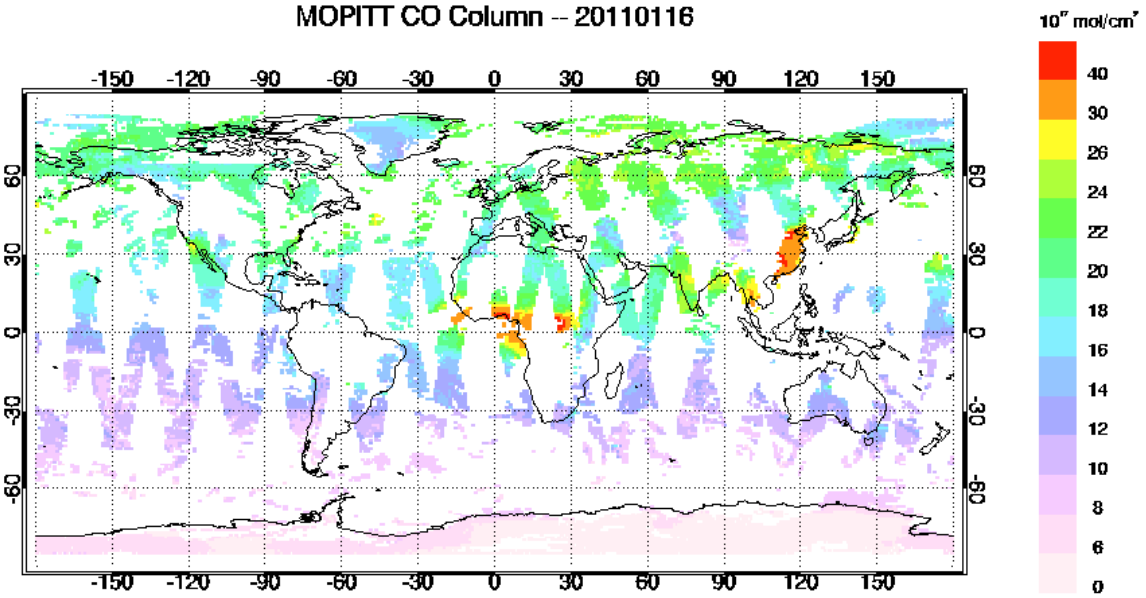
MOPITT CO Column -- 20110116
10^18 mol/cm^2
40
30
26
24
22
20
18
16
14
12
10
8
6
0
-150 -120 -90 -60 -30 0 30 60 90 120 150
60
30
0
-30
-60

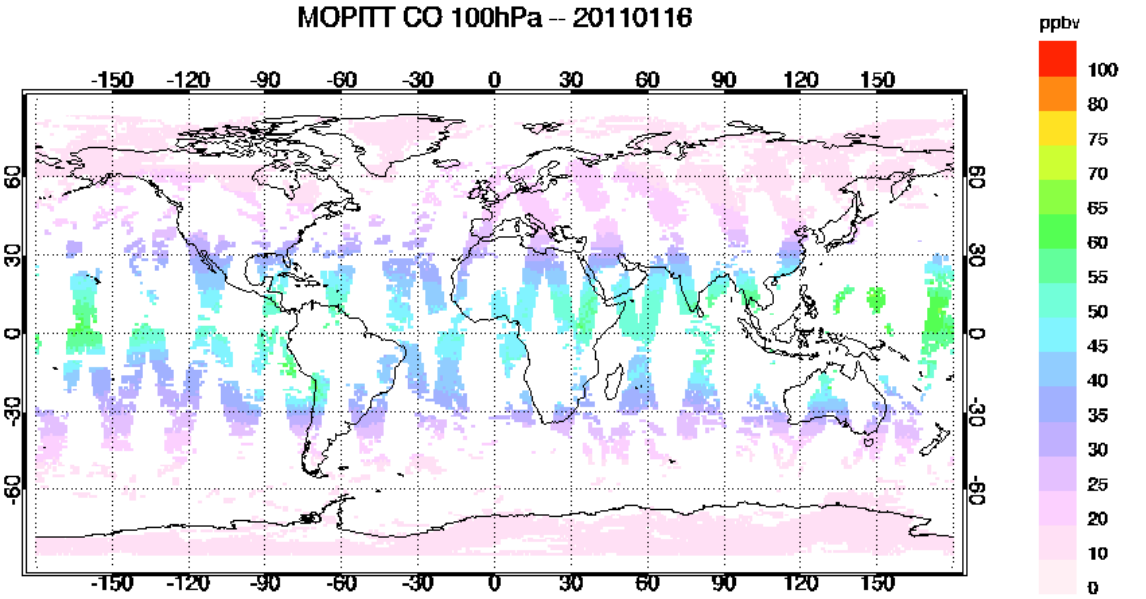
MOPITT CO 100hPa -- 20110116
ppbv
100
80
75
70
65
60
55
50
45
40
35
30
25
20
10
0
-150 -120 -90 -60 -30 0 30 60 90 120 150
60
30
0
-30
-60

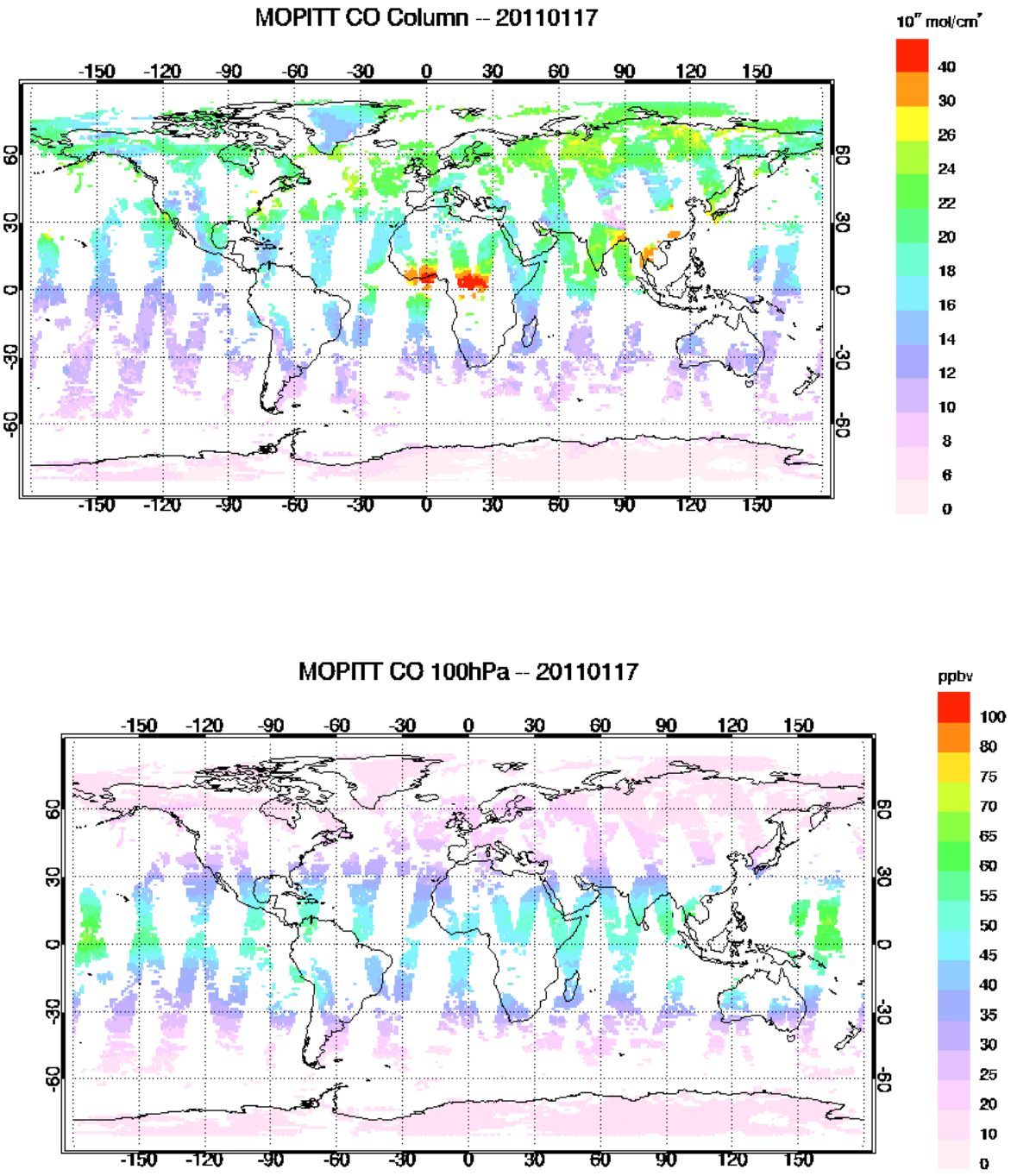

Figure 6.9: carbon monoxide(CO) at different level on the men shined date shown on each panel.

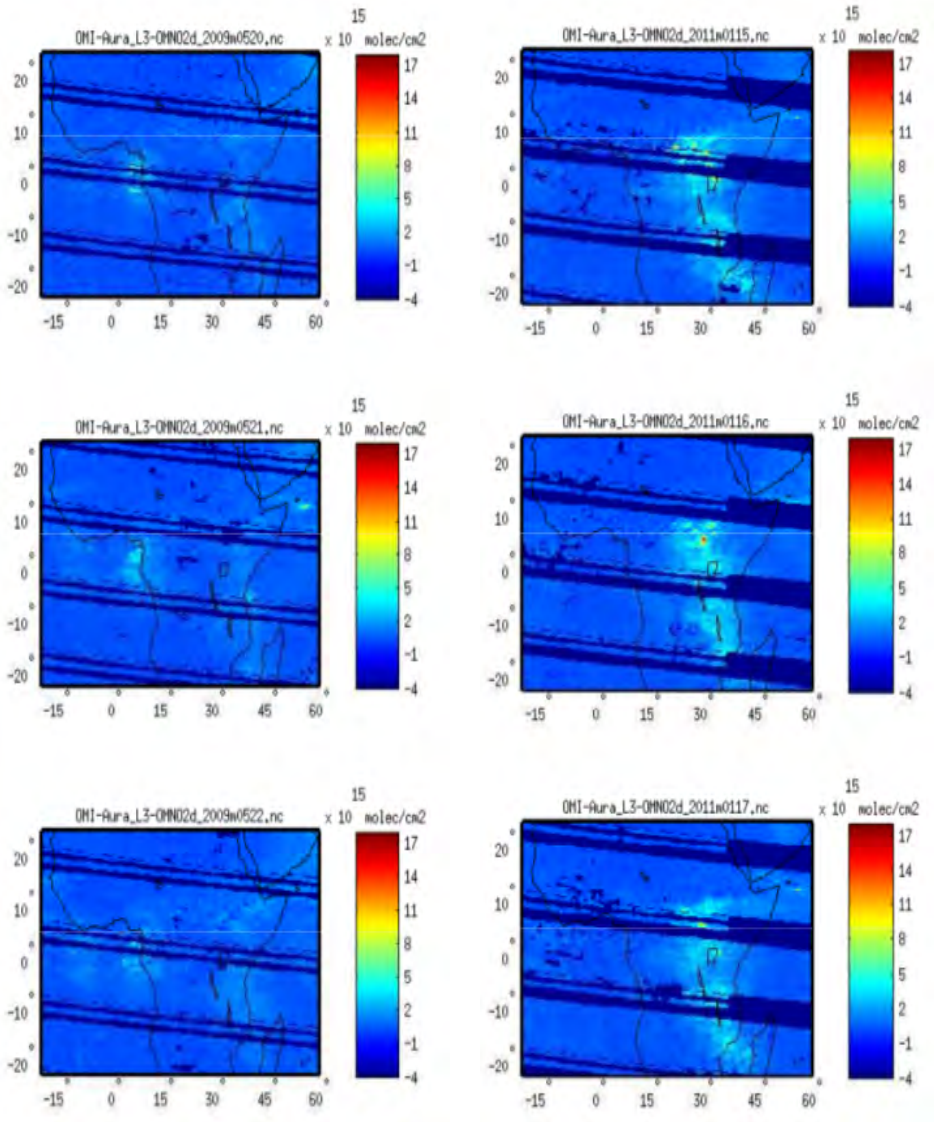

Figure 6.10: NO_2 concentration during the period shown on each panel.

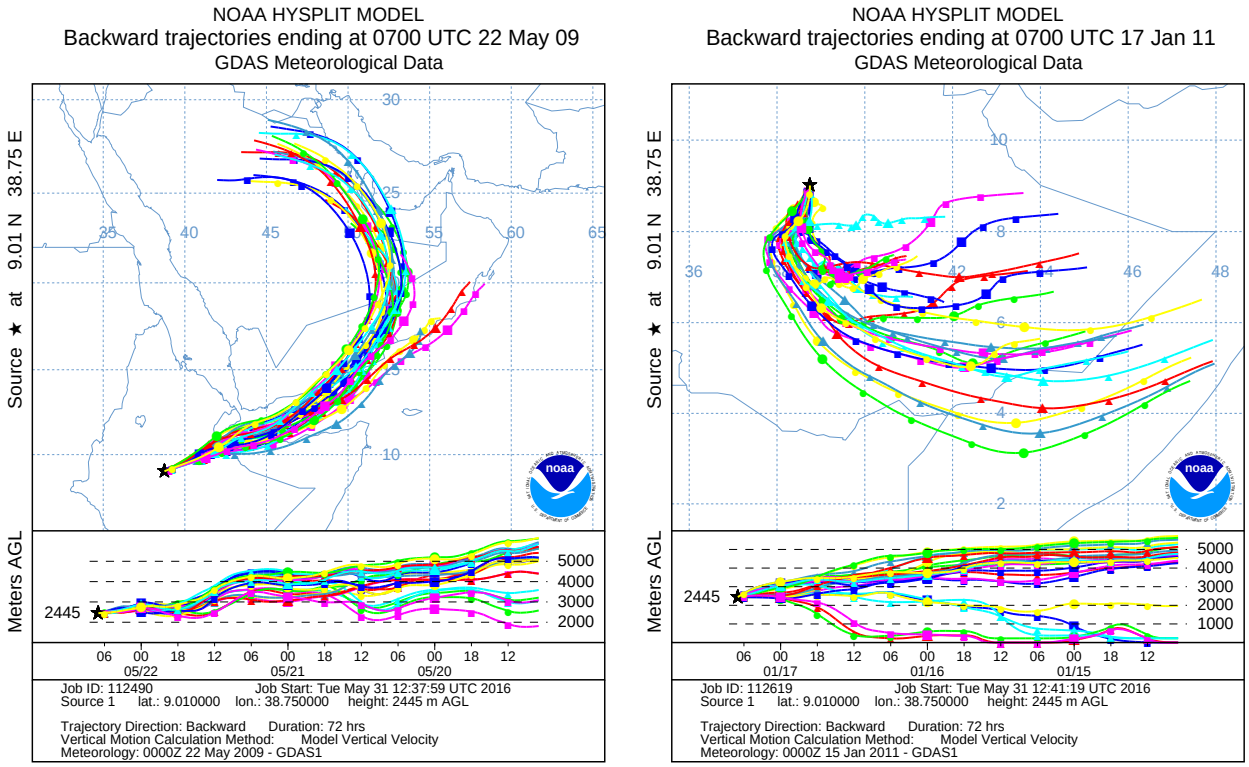

Figure 6.11: Three days back trajectory of the air mass for the enhancement observed on May-22-2009 & January-17-2011 Retrieved from [55].

6.6 Seasonal Variation of TCO and Ozone Mixing Ratio in the Troposphere

Satellite inter comparison of the TCO haves shown more or less a similar pattern regardless of the years. In general, elevated ozone have been recorded during spring and low ozone during summer. A closer look at the spring and the summer seasons show variations among the years. The maximum O_3 column amount and VMR are recorded in March 2013, $\sim 8.5 \times 10^{17} molecule/cm^2$ and 60 ppbv, respectively. Similarily, the OMI measurement shows a maximum value of $1.1 \times 10^{18} molecule/cm^2$ across the tropical Africa during March 2013 and $\sim 9.0 \times 10^{17} molecule/cm^2$ at Addis Ababa. June of 2011 has the greatest column amount, $\sim 8 \times 10^{17} molecule/cm^2$. But the trend of all the month from June to August is almost the same. This is further strengthened by the contour plots of both the Summer season and the Spring season (see Fig. 6.17-6.20).

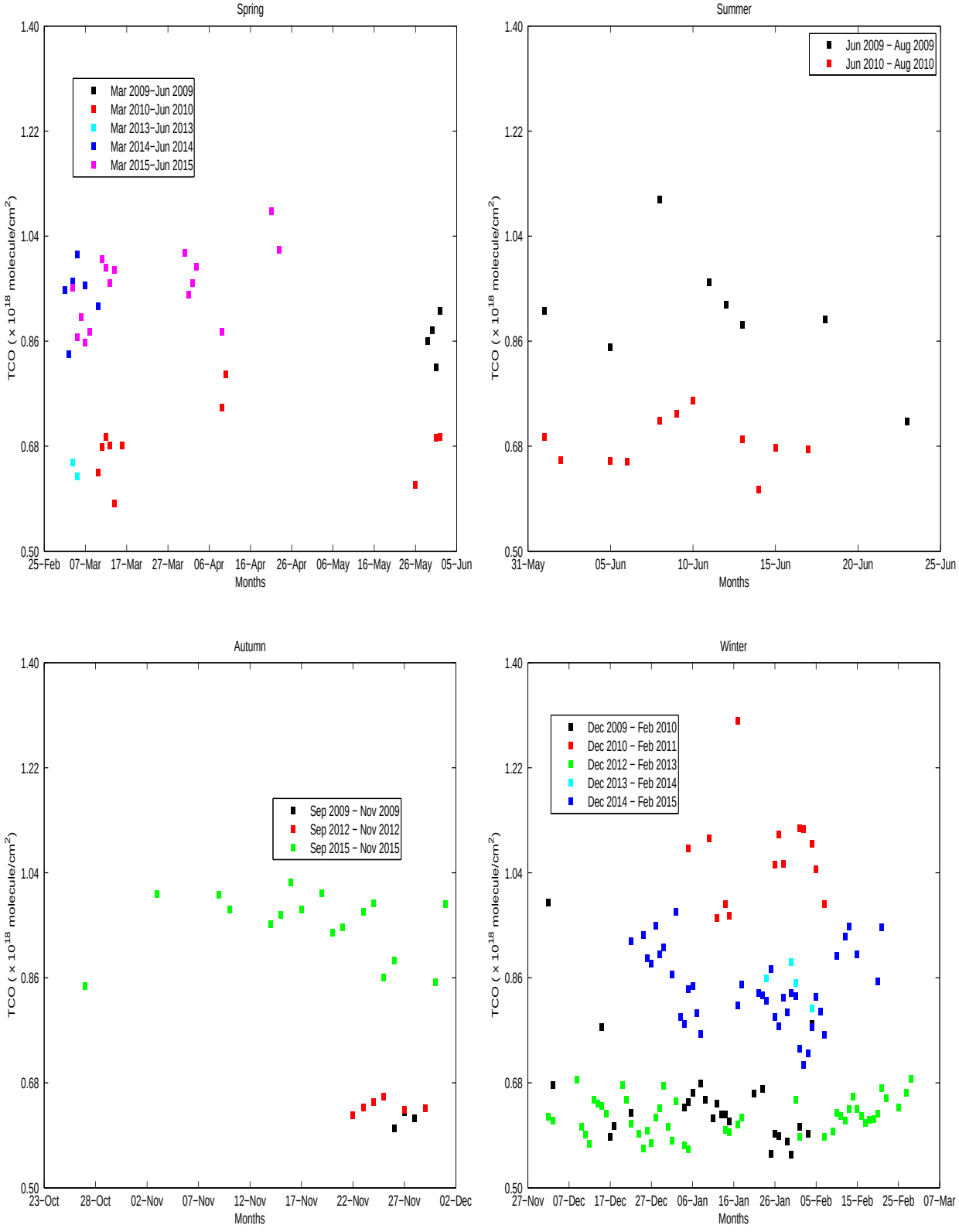

Figure 6.12: TCO Comparison among seasons from FTIR observation.

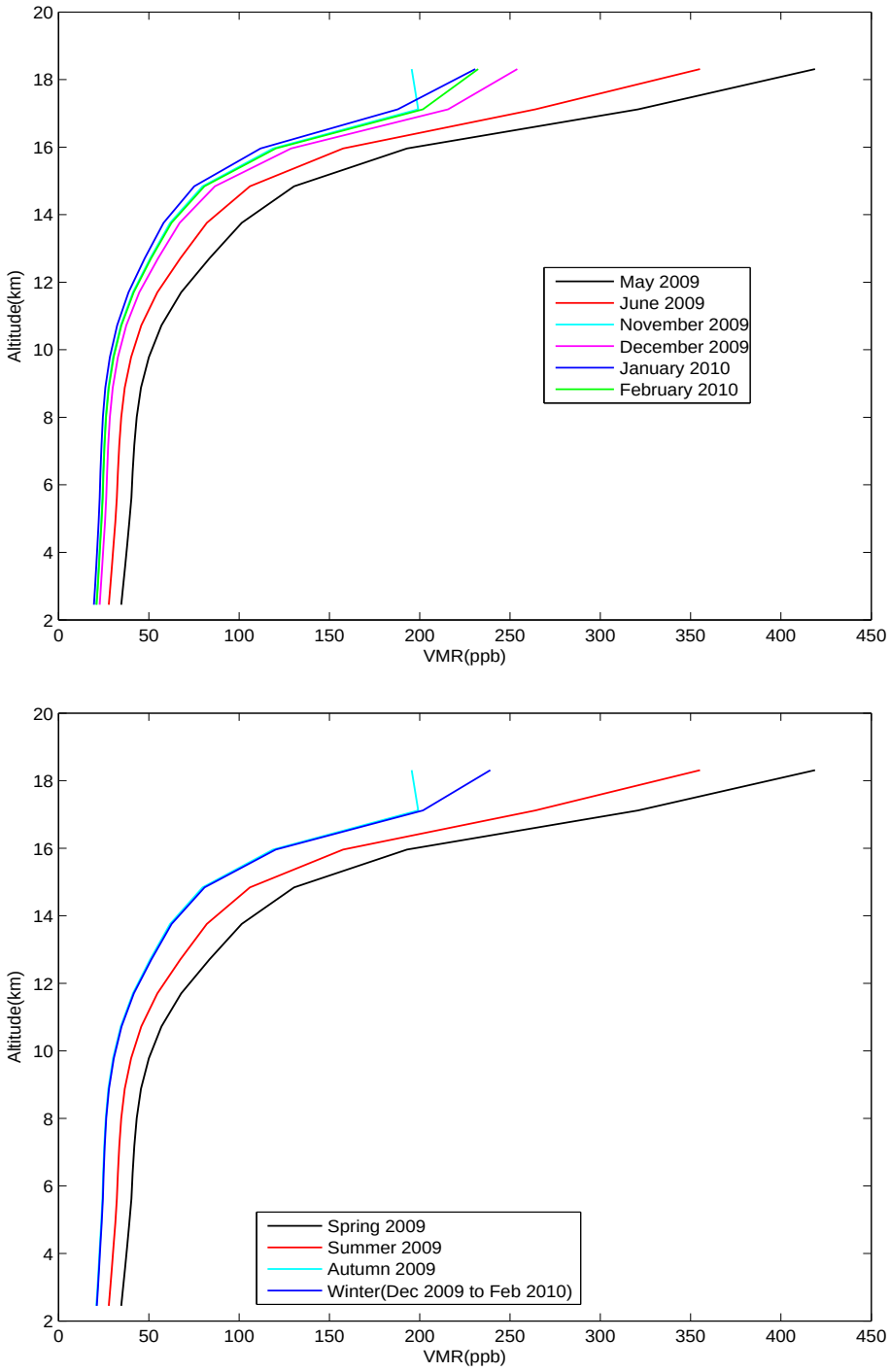

Figure 6.13: Upper: monthly averages of O_3 mixing comparison. lower: seasonal variation of O_3 mixing ratio.

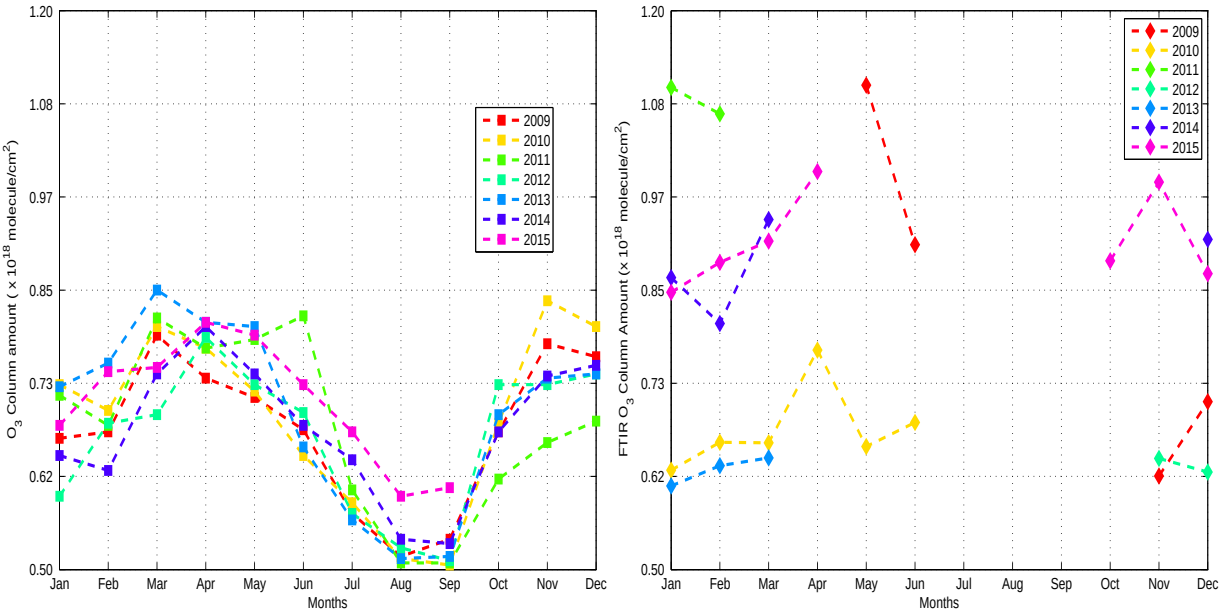

Figure 6.14: Left panel: monthly averages of TCO from OMI/Aura satellite. Right panel: monthly averages of TCO from FTIR.

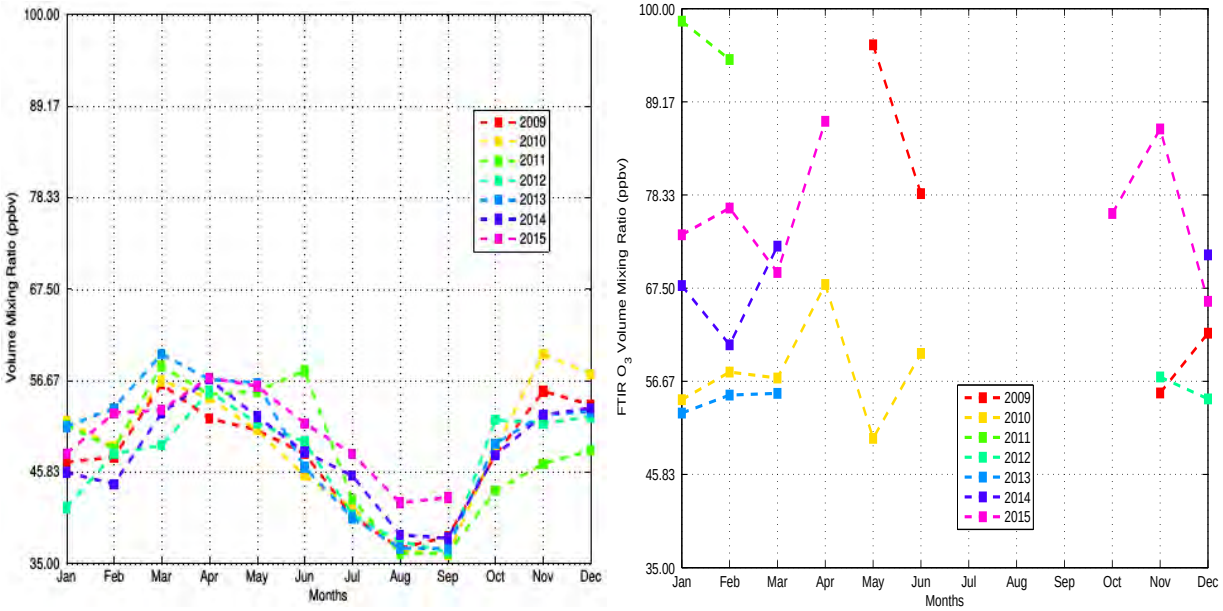

Figure 6.15: Left panel: monthly averages of O_3 VMR from OMI/Aura satellite. Right panel: monthly averages of O_3 VMR from FTIR.

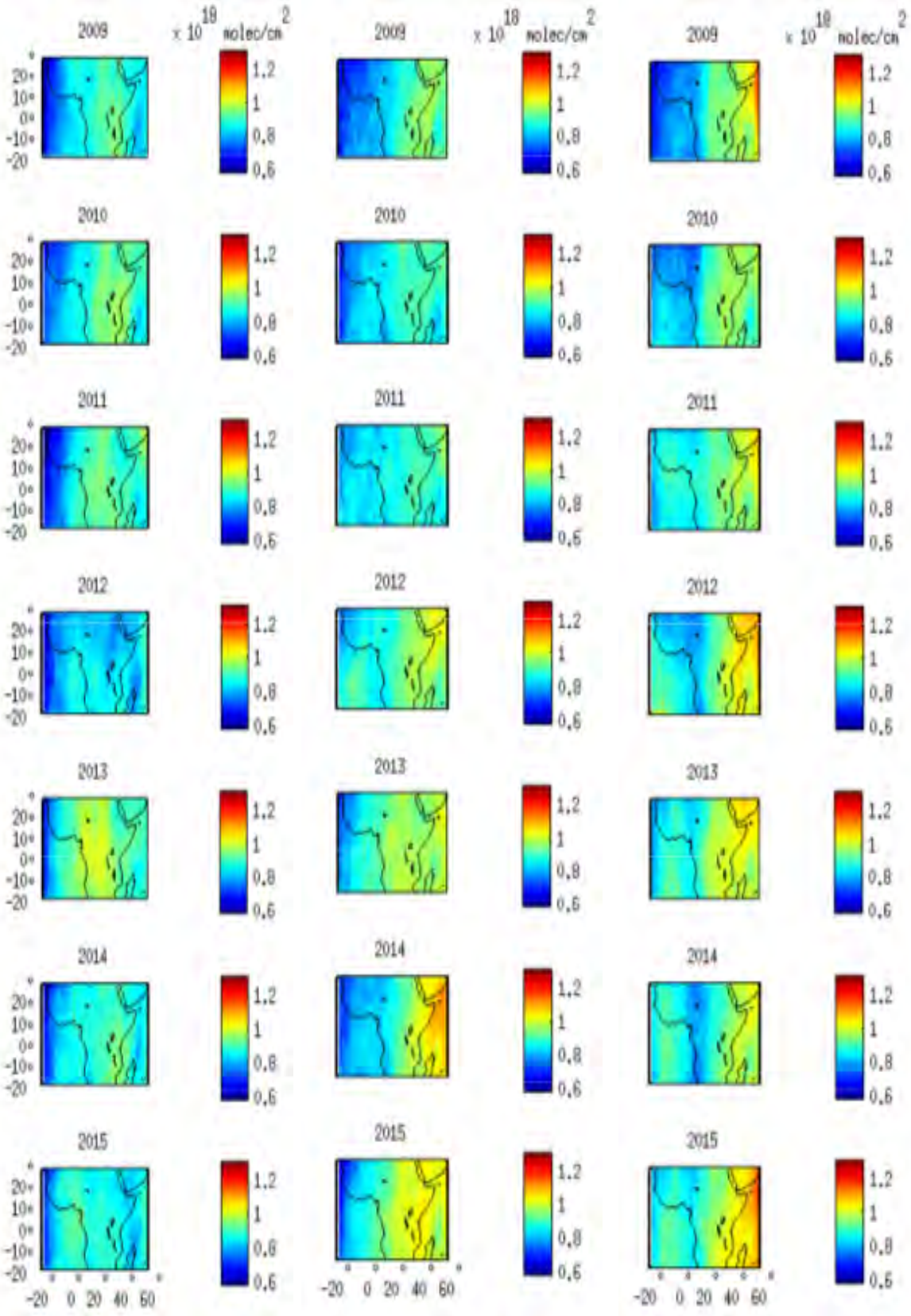

Figure 6.16: TCO variation in spring from 2009 to 2015.

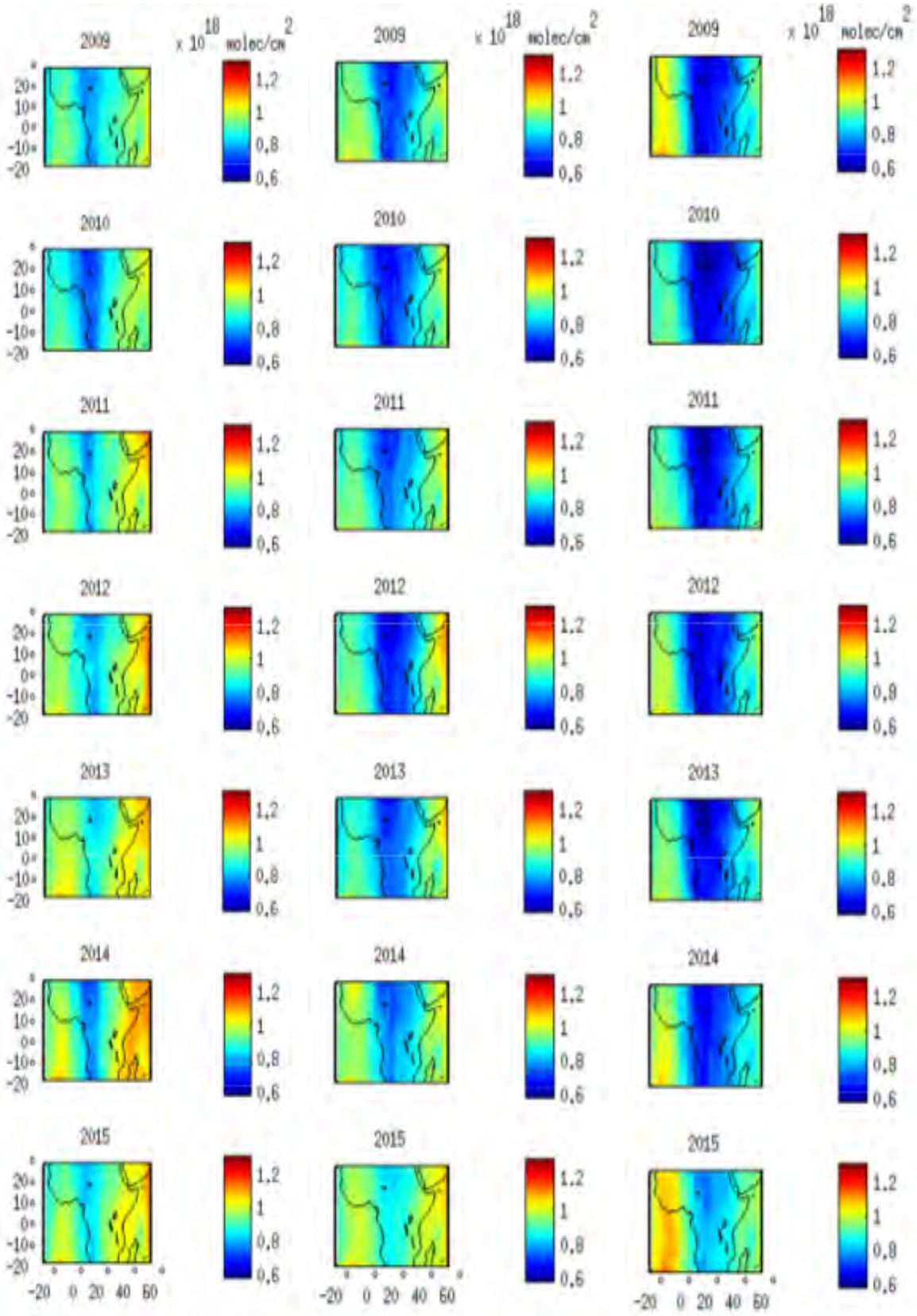

Figure 6.17: TCO variation in summer from 2009 to 2015.

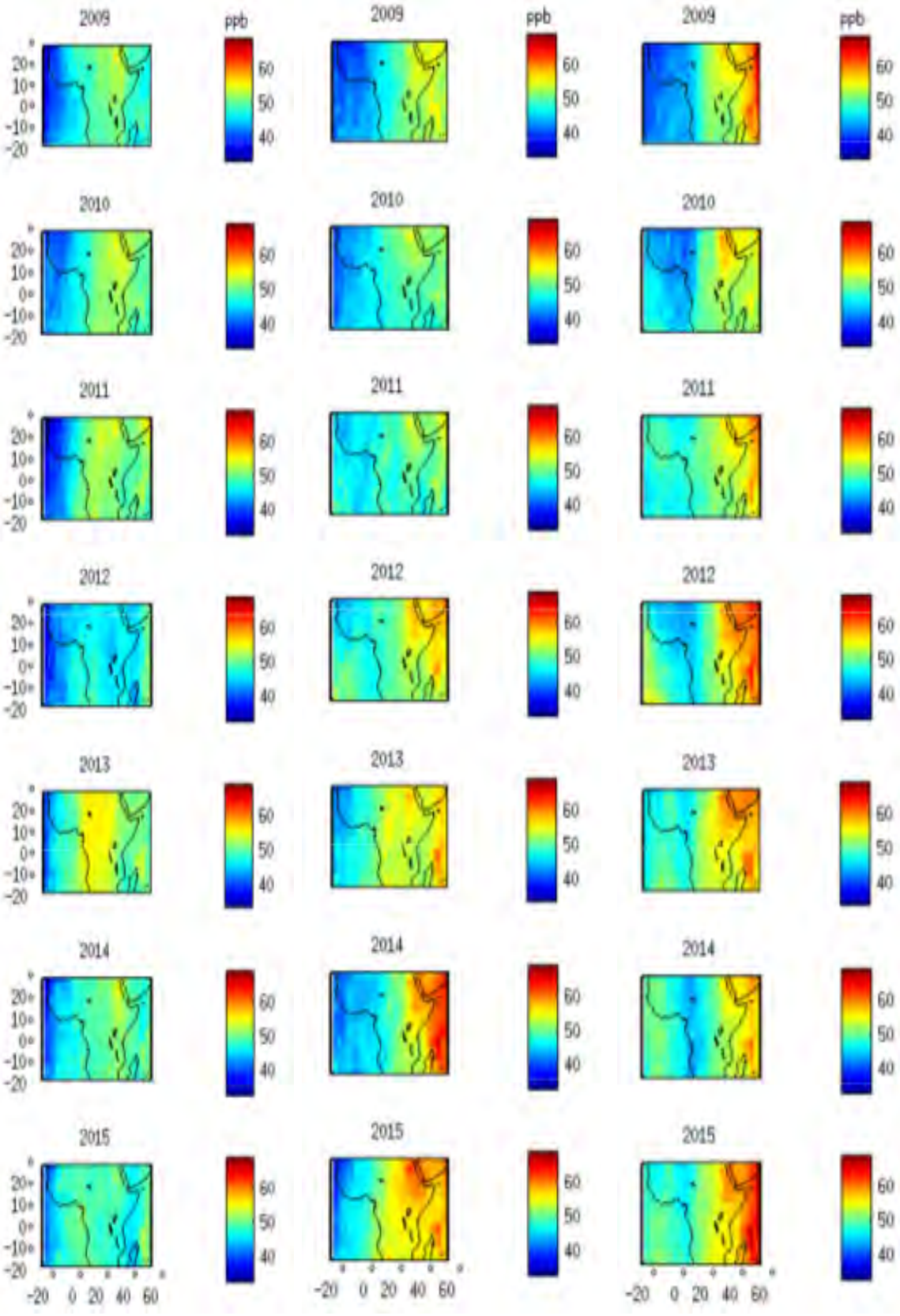

Figure 6.18: VMR variation in spring from 2009 to 2015.

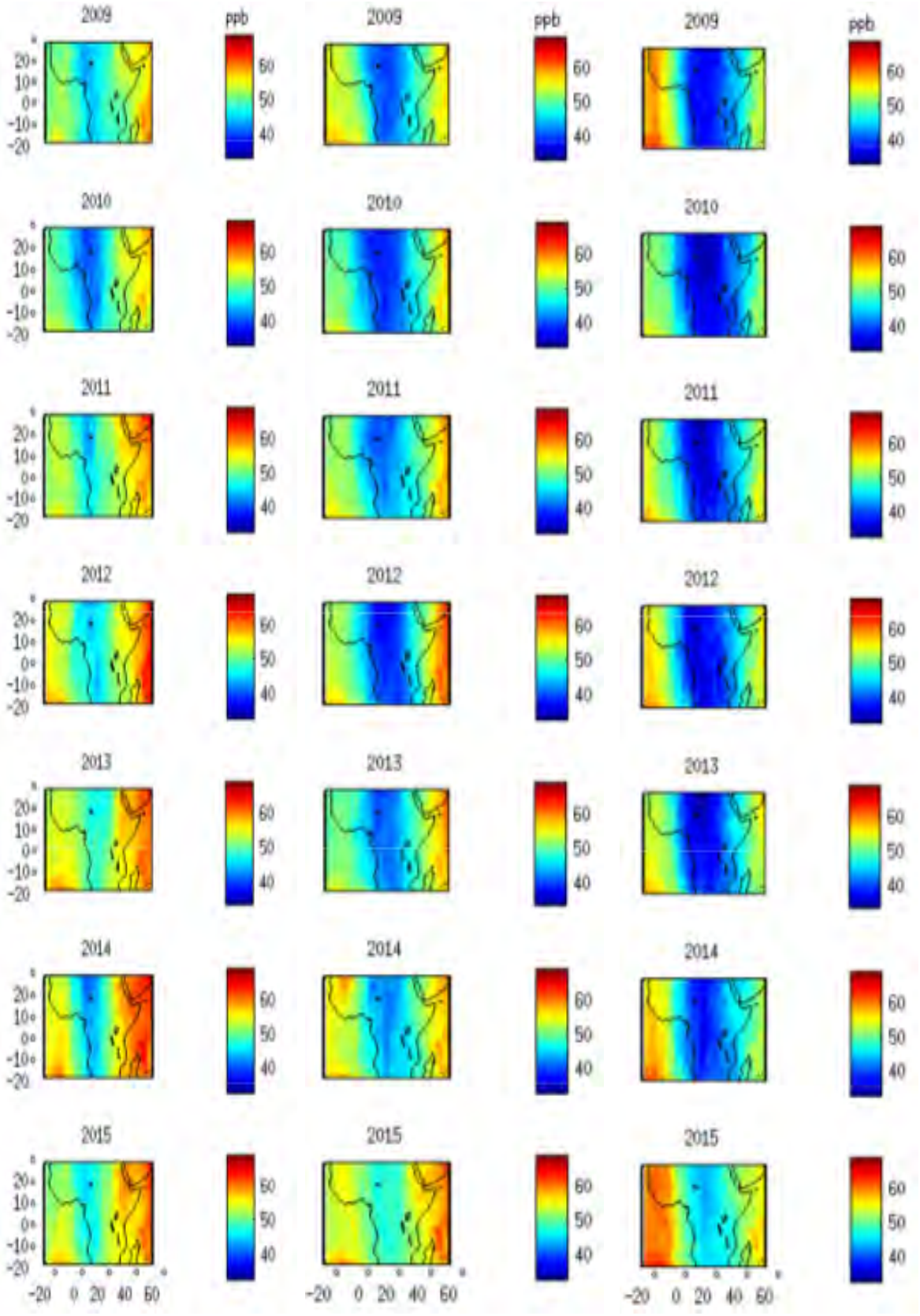

Figure 6.19: VMR variation in summer from 2009 to 2015.

6.7 Error Analysis

Fig. 6.21 shows statistical and systematic errors. The noise, baseline and solar line error contributions are relatively high when compared to the others at lower altitude but at the upper altitude noise, solar line and temperature error have high statistical error contributions. Where as spectroscopic, baseline and ILS error in the lower altitude and spectroscopic, baseline and temperature error in the upper altitude major contributors to the systematic error. Some of the estimated error values for some layers are summarized in Tabls 6.6-6.7

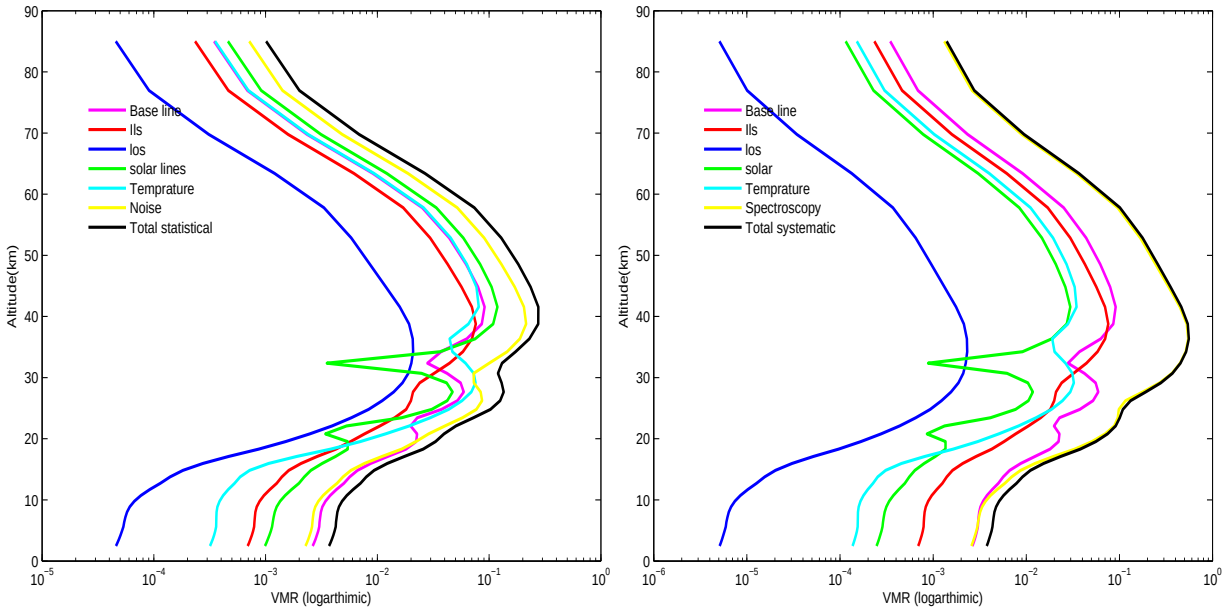

Figure 6.20: Left: altitude variation of statistical error and right: systematic error.

Table 6.5: Statistical error budget for the retrieval of O_3 VMR profile.(%)

Altitude (km)	Baseline	ILS	LOS	Solar Lines	Tmp	Noise	TotalSta
0-2.45	11.96	3.14	0.21	4.48	1.44	10.31	16.78
2.45-2.94	11.96	3.13	0.21	4.48	1.44	10.31	16.77
4.896-5.620	11.77	3.08	0.21	4.46	1.41	10.15	16.53
5.620-6.380	11.66	3.04	0.21	4.44	1.39	10.05	16.36
17.12-18.31	4.37	1.03	0.21	1.32	0.93	4.00	6.23
18.31-19.54	3.11	0.81	0.21	0.76	0.98	3.09	4.63
69.77-76.95	1.52	1.03	0.20	2.02	1.55	3.13	4.44
76.95-85.00	1.52	1.02	0.20	2.02	1.55	3.13	4.44

Table 6.6: systematic error budget for the retrieval of O_3 VMR profile(%).

Altitude (km)	Baseline	ILS	LOS	Solar Lines	Tmp	Spectr	TotalSyst
0-2.45	11.96	3.14	0.02	1.12	0.62	11.68	17.06
2.45-2.94	11.96	3.13	0.02	1.12	0.62	11.68	17.06
4.896-5.620	11.77	3.08	0.02	1.11	0.60	11.66	16.90
5.620-6.380	11.66	3.04	0.02	1.11	0.59	11.64	16.80
17.12-18.31	4.37	1.03	0.02	0.33	0.40	8.04	9.23
18.31-19.54	3.11	0.81	0.02	0.19	0.42	7.10	7.80
69.77-76.95	1.52	1.03	0.02	0.51	0.67	5.79	6.13
76.95-85.00	1.52	1.02	0.02	0.51	0.67	5.79	6.13

Chapter 7

Conclusions

The TCO derived from 236 measurement spectra under the condition of clear sky from May 2009 to Dec 2015 are investigated with respect their comparability with those from satellites, unusual enhancements, and for climatology patterns over equatorial Africa. The tropospheric ozone obtained from the satellite is the difference between the total column of the OMI/Aura with the stratospheric column obtained from MLS/Aura. The minimum and maximum observations of TCO are in May 22, 2009 and January 17, 2011 respectively. In general, elevated ozone have been recorded during spring and low ozone during summer. A closer look at the spring and the summer seasons show variations among the years. The maximum O_3 column amount and VMR are recorded in March 2013, $\sim 8.5 \times 10^{17} molecule/cm^2$ and 60 ppbv respectively. June of 2011 has the greatest column amount, $\sim 8 \times 10^{17} molecule/cm^2$. But the trend of all the month from June to August is almost the same. Comparisons of TCOs from FTIR and satellites shows large discrepancy with respect absolute magnitudes. The discrepancy might be related to difference in spectral range used to drive TCO. The satellite uses strong UV-visible spectral region while FTIR uses microwindow from mid-infrared which is relatively contaiminated by interfering species. The observation geometry has also some roles. However, FTIR and satellite observations agree with respect to seasonality and enhanced TCO cases.

Bibliography

[1] Samuel, T.(2007). IMPACT ASSESSMENT OF UNCERTAINTY OF SPECTROSCOPIC PARAMETERS ON THE ACCURACY OF TRACE GASES ABUNDANCE (Unpublished master's thesis, Physics Department, Addis Ababa University, Ethiopia) Retrieved from http://hdl.handle.net/123456789/1392.

[2] Gezahegn, S. (2010). Observation of Atmospheric Carbon Monoxide by Ground-Based FTIR Spectrometer over Addis Ababa, Ethiopia (Unpublished master's thesis, Physics Department, Addis Ababa University, Ethiopia) Retrieved from http://hdl.handle.net/123456789/1220.

[3] FRIEWELEGA, G. (2011). OBSERVATION AND VALIDATION OF NO AND NO2 FROM FTIR OVER ADDIS ABABA (Unpublished master's thesis, Physics Department, Addis Ababa University, Ethiopia) Retrieved from http://hdl.handle.net/123456789/1287.

[4] Kgabi, N. A., & Sehloho, R. M. (2012). Seasonal variations of tropospheric ozone concentrations. Global Journal of Science Frontier Research, 12(5-B).

[5] Endale, G. (2011). OBSERVATION AND VALIDATION OF METHANE FROM FT-IR OVER ADDIS ABABA (Unpublished master's thesis, Physics Department, Addis Ababa University, Ethiopia) Retrieved from http://hdl.handle.net/123456789/1288.

[6] Salby, M. L. (1996). Fundamentals of atmospheric physics (Vol. 61). Academic press.

[7] Jacob, D. (1999). Introduction to atmospheric chemistry. Princeton University Press.

[8] Seinfeld, J. H., & Pandis, S. N. (2016). Atmospheric chemistry and physics: from air pollution to climate change. John Wiley & Sons.

[9] Christopherson, R. W. (2013). Elemental geosystems. Pearson Education.

[10] Salby, M. L. (2012). Physics of the Atmosphere and Climate. Cambridge University Press.

[11] Holton, J. R., Haynes, P. H., McIntyre, M. E., Douglass, A. R., Rood, R. B., & Pfister, L. (1995). Stratospheretroposphere exchange. Reviews of geophysics, 33(4), 403-439.

[12] MILKESSA, G. H. (2010). Stratospheric Aerosol Climatology From Sage II and Observation of its Deriver, Carbonyl Sulfide, Over Equatorial Africa Unpublished master's thesis, Physics Department, Addis Ababa University, Ethiopia) Retrieved from http://hdl.handle.net/123456789/1196.

[13] Newman, P. A., & Morris, G. (2003). Stratospheric Ozone; An Electronic Textbook. Studying Earths Environment From Space. NASA, 480.

[14] Raghunandan, A., Mahumane, G., & Diab, R. (2007). Elevated ozone events over Johannesburg based on analysis of tropospheric ozone partial columns. South African Journal of Science, 103(5/6), 248.

[15] Kassahun, T. (2011). OZONE DYNAMICS AND SEASONAL VARIABILITY OVER AFRICA (Doctoral dissertation, aau).

[16] Ziemke, J. R., Chandra, S., Duncan, B. N., Froidevaux, L., Bhartia, P. K., Levelt, P. F., & Waters, J. W. (2006). Tropospheric ozone determined from Aura OMI and MLS: Evaluation of measurements and comparison with the Global Modeling Initiative's Chemical Transport Model. Journal of Geophysical Research: Atmospheres, 111(D19).

[17] Monks, P. S., Archibald, A. T., Colette, A., Cooper, O., Coyle, M., Derwent, R., ... & Stevenson, D. S. (2015). Tropospheric ozone and its precursors from the urban to the global scale from air quality to short-lived climate forcer. Atmospheric Chemistry and Physics, 15(15), 8889-8973.

[18] Hsu, J., & Prather, M. J. (2009). Stratospheric variability and tropospheric ozone. Journal of Geophysical Research: Atmospheres, 114(D6).

[19] Stohl, A., Bonasoni, P., Cristofanelli, P., Collins, W., Feichter, J., Frank, A., ... & Kentarchos, T. (2003). Stratospheretroposphere exchange: A review, and what we have learned from STACCATO. Journal of Geophysical Research: Atmospheres, 108(D12).

[20] Fry, M. M., Naik, V., West, J. J., Schwarzkopf, M. D., Fiore, A. M., Collins, W. J., ... & Duncan, B. N. (2012). The influence of ozone precursor emissions from four world regions on tropospheric composition and radiative climate forcing. Journal of Geophysical Research: Atmospheres, 117(D7).

[21] Monks, P. S., Archibald, A. T., Colette, A., Cooper, O., Coyle, M., Derwent, R., ... & Stevenson, D. S. (2015). Tropospheric ozone and its precursors from the urban to the global scale from air quality to short-lived climate forcer. Atmospheric Chemistry and Physics, 15(15), 8889-8973.

[22] Galbally, I.E.; Cope, M. E.; Lawson, S. J.; Bentley, S.T.; Cheng, M.; Gillett, ... & S.; Hodge, M. (2008). Sources of Ozone Precursors and Atmospheric Chemistry in a Typical Australian City. CSIRO, 17.

[23] István, L., Róbert, M., Györgyi, G., Ádám, L. (2013). Atmospheric Chemistry. Eötvös Loránd University. pp 83-84.

[24] Seidel, D. J., Ross, R., Angell, J. K., & Reid, G. C. (2001). Climatological characteristics of the tropical tropopause as revealed by radiosondes. Journal of Geophysical Research, 106(D8), 7857-7878.

[25] Marufu, L., Dentener, F., Lelieveld, J., Andreae, M. O., & Helas, G. (2000). Photochemistry of the African troposphere: Influence of biomass-burning emissions. Journal of Geophysical Research: Atmospheres, 105(D11), 14513-14530.

[26] Crutzen, P. J., & Andreae, M. O. (1990). Biomass burning in the tropics: impact on atmospheric chemistry and biogeochemical cycles. Science, 250(4988), 1669-1678.

[27] Sauvage, B., Thouret, V., Cammas, J. P., Gheusi, F., Athier, G., & Ndlec, P. (2005). Tropospheric ozone over Equatorial Africa: regional aspects from the MOZAIC data. Atmospheric Chemistry and Physics, 5(2), 335.

[28] Jonquires, I., Marenco, A., Maalej, A., & Rohrer, F. (1998). Study of ozone formation and transatlantic transport from biomass burning emissions over West Africa during the airborne Tropospheric Ozone Campaigns TROPOZ I and TROPOZ II. Journal of Geophysical Research: Atmospheres, 103(D15), 19059-19073.

[29] Aghedo, A. M., Schultz, M. G., & Rast, S. (2007). The influence of African air pollution on regional and global tropospheric ozone. Atmospheric Chemistry and Physics, 7(5), 1193-1212.

[30] Murphy, J. G., Oram, D. E., & Reeves, C. E. (2010). Measurements of volatile organic compounds over West Africa. Atmospheric Chemistry and Physics, 10(12), 5281-5294.

[31] Real, E., Orlandi, E., Law, K. S., Fierli, F., Josset, D., Cairo, F., ... & McQuaid, J. B. (2010). Cross-hemispheric transport of central African biomass burning pollutants: implications for downwind ozone production. Atmospheric Chemistry and Physics, 10(6), 3027-3046.

[32] Jaegl, L., Steinberger, L., Martin, R. V., & Chance, K. (2005). Global partitioning of NO_x sources using satellite observations: Relative roles of fossil fuel combustion, biomass burning and soil emissions. Faraday discussions, 130, 407-423.

[33] Galy-Lacaux, C., Laouali, D., Descroix, L., Gobron, N., & Liousse, C. (2009). Long term precipitation chemistry and wet deposition in a remote dry savanna site in Africa (Niger). Atmospheric Chemistry and Physics, 9(5), 1579-1595.

[34] Fineberg, N. A., Potenza, M. N., Chamberlain, S. R., Berlin, H. A., Menzies, L., Bechara, A., ... & Hollander, E. (2010). Probing compulsive and impulsive behaviors, from animal models to endophenotypes: a narrative review. Neuropsychopharmacology, 35(3), 591-604.

[35] Minga, A., Thouret, V., Saunois, M., Delon, C., Sera, D., Mari, C., ... & Cros, B. (2010). What caused extreme ozone concentrations over Cotonou in December 2005?. Atmospheric Chemistry and Physics, 10(3), 895-907.

[36] Martin, R. V., Sauvage, B., Folkins, I., Sioris, C. E., Boone, C., Bernath, P., & Ziemke, J. (2007). Spacebased constraints on the production of nitric oxide by lightning. Journal of Geophysical Research: Atmospheres, 112(D9).

[37] Barrett, T. J., & Munkittrick, K. R. (2010). Seasonal reproductive patterns and recommended sampling times for sentinel fish species used in environmental effects monitoring programs in Canada. Environmental Reviews, 18(NA), 115-135.

[38] Bouarar, I., Law, K. S., Pham, M., Liousse, C., Schlager, H., Hamburger, T., ... & Ravegnani, F. (2011). Emission sources contributing to tropospheric ozone over Equatorial Africa during the summer monsoon. Atmospheric Chemistry and Physics, 11(24), 13395-13419.

[39] Mari, C. H., Cailley, G., Corre, L., Saunois, M., Atti, J. L., Thouret, V., & Stohl, A. (2008). Tracing biomass burning plumes from the Southern Hemisphere during the AMMA 2006 wet season experiment. Atmospheric Chemistry and Physics, 8(14), 3951-3961.

[40] Liu, A., Tegmark, M., Bowman, J., Hewitt, J., & Zaldarriaga, M. (2009). An improved method for 21-cm foreground removal. Monthly Notices of the Royal Astronomical Society, 398(1), 401-406.

[41] Janicot, S., Thorncroft, C. D., Ali, A., Asencio, N., Berry, G. J., Bock, O., ... & Kergoat, L. (2008). Large-scale overview of the summer monsoon over West Africa during the AMMA field experiment in 2006. In Annales Geophysicae (Vol. 26, pp. 2569-2595).

[42] Hariharan, P. (2010). Basics of interferometry. Academic Press.

[43] Al-Hazaimay, S., Schrems, R. P. D. O., & Warneke, T. T. (2008). Impact of Instrumental Parameters on atmospheric Trace Gases Retrievals using FTIR Spectrometry (Doctoral dissertation, MSc. Thesis Institute of Environmental Physics, University of Bremen).

[44] Griffiths, P. R., & De Haseth, J. A. (2007). Fourier transform infrared spectrometry (Vol. 171). John Wiley & Sons.

[45] Smith, B. C. (2011). Fundamentals of Fourier transform infrared spectroscopy. CRC press.

[46] Thermo, N. (2001). Introduction to fourier transform infrared spectrometry. Thermo Nicolet Corporation: Madison-USA.

[47] Reichler, T., Dameris, M., & Sausen, R. (2003). Determining the tropopause height from gridded data. Geophysical research letters, 30(20).

[48] Takele Kenea, S., Mengistu Tsidu, G., Blumenstock, T., Hase, F., Clarmann, T. V., & Stiller, G. P. (2013). Retrieval and satellite intercomparison of O_3 measurements from ground-based FTIR Spectrometer at Equatorial Station: Addis Ababa, Ethiopia. Atmospheric Measurement Techniques, 6(2), 495-509.

[49] Rodgers, C. D. (2000). Inverse methods for atmospheric sounding: theory and practice (Vol. 2). World scientific.

[50] Aster, R. C., Borchers, B., & Thurber, C. Parameter Estimation and Inverse Problems. 2005.

[51] Steck, T., & Clarmann, T. V. (2000). Constrained Profile Retrieval Applied to MIPAS Observation Mode.

[52] Hansen, P. C. (1992). Analysis of discrete ill-posed problems by means of the L-curve. SIAM review, 34(4), 561-580.

[53] Dudhia, A., & Dinelli, B. M. (1997). Optimisation of the Atmospheric Vertical Grid. Task 2.2 of ESA.

[54] Golub, G., & Kahan, W. (1965). Calculating the singular values and pseudo-inverse of a matrix. Journal of the Society for Industrial and Applied Mathematics, Series B: Numerical Analysis, 2(2), 205-224.

[55] HYSPLIT (Hybrid Single Particle Lagrangian Integrated Trajectory) Model, http://www.arl.noaa.gov/

Declaration

This thesis is my original work, has not been presented for a degree in any other University and that all the sources of material used for the thesis have been dully acknowledged.

Signature:– – – – – – – – – – –

Place and time of submission: Addis Ababa University, June 2016

This thesis has been submitted for examination with my approval as University advisor.

Name: Prof. Gizaw Mengistu Tsidu

(Bostwana International University of Technology and Science /Addis Ababa University)

Signature:– – – – – – – – – ––